Exportin Crm1 is repurposed as a docking protein to generate microtubule organizing centers at the nuclear pore

Xun X. Bao[1], Christos Spanos[1], Tomoko Kojidani[2,3], Eric M. Lynch[1]*, Juri Rappsilber[1,4], Yasushi Hiraoka[2,5], Tokuko Haraguchi[2,5], and Kenneth E. Sawin[1]**

1.Wellcome Centre for Cell Biology, School of Biological Sciences, University of Edinburgh, Michael Swann Building, Max Born Crescent, Edinburgh EH9 3BF, UK

2. Advanced ICT Research Institute Kobe, National Institute of Information and Communications Technology, Kobe, Japan

3 Department of Chemical and Biological Sciences, Faculty of Science, Japan Women's University, Tokyo, Japan

4. Chair of Bioanalytics, Institute of Biotechnology, Technische Universität Berlin, Berlin, 13355, Germany

5. Graduate School of Frontier Biosciences, Osaka University, Suita, Japan

* *Present address:* Dept. of Biochemistry, University of Washington, 1959 NE Pacific Street, Box 357350, Seattle, WA 98195, USA

** Author for correspondence

ABSTRACT

Non-centrosomal microtubule organizing centers (MTOCs) are important for microtubule organization in many cell types. In fission yeast *Schizosaccharomyces pombe*, the protein Mto1, together with partner protein Mto2 (Mto1/2 complex), recruits the γ-tubulin complex to multiple non-centrosomal MTOCs, including the nuclear envelope (NE). Here, we develop a comparative-interactome mass spectrometry approach to determine how Mto1 localizes to the NE. Surprisingly, we find that Mto1, a constitutively cytoplasmic protein, docks at nuclear pore complexes (NPCs), via interaction with exportin Crm1 and cytoplasmic FG-nucleoporin Nup146. Although Mto1 is not a nuclear export cargo, it binds Crm1 via a nuclear export signal-like sequence, and docking requires both Ran in the GTP-bound state and Nup146 FG repeats. In addition to determining the mechanism of MTOC formation at the NE, our results reveal a novel role for Crm1 and the nuclear export machinery in the stable docking of a cytoplasmic protein complex at NPCs.

INTRODUCTION

Non-centrosomal microtubule organizing centers (MTOCs) are critical to the morphology and function of many types of cells (Petry & Vale, 2015, Sanchez & Feldman, 2017, Wu & Akhmanova, 2017), especially cells in which interphase microtubules (MTs) are arranged in linear rather than radial arrays (Bartolini & Gundersen, 2006). Examples include differentiated animal cells such as neurons (Kapitein & Hoogenraad, 2015), muscle (Mogessie et al., 2015, Tassin et al., 1985), and epithelial cells (Wu & Akhmanova, 2017), and many higher plant cells (Masoud et al., 2013, Oda, 2015), as well as some single-celled eukaryotes, such as fission yeast *Schizosaccharomyces pombe* (Chang & Martin, 2009, Sawin & Tran, 2006).

The mechanisms underlying non-centrosomal MTOC formation are just beginning to be understood. Some non-centrosomal MTs are thought to be generated by nucleation-and-release from the centrosome, followed by minus-end stabilization and anchoring elsewhere in the cell (Bartolini & Gundersen, 2006, Sanchez & Feldman, 2017, Wu & Akhmanova, 2017). However, in many cases MTs are nucleated directly from non-centrosomal sites by the γ-tubulin complex, the primary microtubule-nucleation complex in eukaryotic cells (Kollman et al., 2011, Petry & Vale, 2015). Understanding how the γ-tubulin complex is recruited to these sites is thus key to deciphering the fundamental mechanisms of non-centrosomal MT organization (Lin et al., 2015).

Sites of non-centrosomal γ-tubulin complex recruitment include pre-existing microtubules themselves, as well as membrane-bound compartments such as the Golgi apparatus and the nuclear envelope (NE). Recruitment of the γ-tubulin complex to pre-existing microtubules depends on the multi-subunit augmin complex, in both animals and plants (Goshima et al., 2008, Liu et al., 2014, Sanchez-Huertas et al., 2016). Microtubule nucleation and organization by the Golgi apparatus is orchestrated largely by AKAP450, which recruits not only the γ-tubulin complex but also its activators, as well as MT minus-end stabilizers (Rivero et al., 2009, Wu et al., 2016). Combined recruitment of γ-tubulin complex and MT minus-end stabilizers/anchoring proteins is also important for MTOC organization at the cell cortex in diverse types of epithelial cells (summarized in (Sanchez & Feldman, 2017, Wu & Akhmanova, 2017)).

MTOC formation at the NE remains poorly understood. The NE is an important MT nucleation site both in muscle cells (Tassin et al., 1985) and in higher plants (Ambrose & Wasteneys, 2014, Masoud et al., 2013, Stoppin et al., 1994), as well as in fission yeast (Lynch et al., 2014, Sawin & Tran, 2006). In muscle, γ-tubulin complex components and associated proteins are redistributed from the centrosome to the NE during development/differentiation, coincident with a decrease in centrosomal MT nucleation and

77   large-scale changes in intracellular MT organization (Bugnard et al., 2005, Fant et al., 2009,

78   Srsen et al., 2009, Zebrowski et al., 2015). In plant cells, which lack centrosomes

79   altogether, many of the same proteins are similarly observed on the NE, especially before

80   and/or after cell division (Erhardt et al., 2002, Janski et al., 2012, Nakamura et al., 2012,

81   Seltzer et al., 2007). However, the mechanisms that regulate their recruitment are largely a

82   mystery.

83   Fission yeast nucleate MTs from multiple non-centrosomal sites through the cell

84   cycle and thus provide an excellent system to study non-centrosomal MTOCs, including

85   those on the NE (Sawin & Tran, 2006). During interphase, linear arrays of MTs are

86   nucleated from the spindle pole body (SPB; the yeast centrosome equivalent), from MTOCs

87   on the NE and on pre-existing microtubules, and from "free" MTOCs in the cytoplasm. As

88   cells enter mitosis, non-centrosomal MT nucleation is switched off (Borek et al., 2015) and

89   the duplicated SPBs become the only active MTOCs, nucleating both intranuclear spindle

90   MTs and cytoplasmic astral MTs. Towards the end of cell division, microtubules are

91   nucleated from the cytokinetic actomyosin ring (CAR). By contrast, in budding yeast

92   *Saccharomyces cerevisiae*, the SPBs are the only MTOCs throughout the cell cycle.

93   In fission yeast, all MT nucleation in the cytoplasm (i.e. both centrosomal and non-

94   centrosomal nucleation) depends on the Mto1/2 complex (Janson et al., 2005, Samejima et

95   al., 2005, Sawin et al., 2004, Venkatram et al., 2005, Venkatram et al., 2004)*. Mto1/2

96   contains multiple copies of the proteins Mto1 and Mto2 and directly recruits the γ-tubulin

97   complex to prospective MTOC sites. Mto1/2 interacts with the γ-tubulin complex via Mto1's

98   Centrosomin Motif 1 (CM1) domain, which is conserved in higher eukaryotic MTOC

99   regulators such as *Drosophila* centrosomin, and human CDK5RAP2 and myomegalin

100   (Samejima et al., 2008, Sawin et al., 2004, Zhang & Megraw, 2007). Interaction of CM1-

101   domain proteins with the γ-tubulin complex can also serve to activate the γ-tubulin complex

102   (Choi et al., 2010, Lynch et al., 2014), although the detailed mechanisms remain unclear.

103   Because Mto1/2 localizes to prospective MTOC sites independently of interacting

104   with the γ-tubulin complex (Samejima et al., 2008), Mto1/2 localization effectively determines

105   where and when all cytoplasmic MTOCs are generated, and thus understanding Mto1/2

106   localization is critical to understanding MTOC formation more broadly. Mto1/2 localization is

107   mediated primarily by domains within Mto1 (Fig. 1A; (Samejima et al., 2010)), although Mto2

108   contributes indirectly by helping to multimerize the Mto1/2 complex (Lynch et al., 2014,

109   Samejima et al., 2005). Mto1/2 association with pre-existing MTs depends on a broadly

110   defined region near the Mto1 C-terminus, while localization to the CAR and the SPB is

111   mediated by overlapping modular sequences within the conserved MASC domain at the

112   Mto1 C-terminus (Samejima et al., 2010). Localization to the CAR involves interaction of

113   MASC with the unconventional myosin Myp2, while localization to the SPB involves the

114   Septation Initiation Network protein Cdc11 (Samejima et al., 2010).

115   Here we determine the mechanism of Mto1/2 localization to the NE. Using a

116   comparative-interactome mass spectrometry approach, we find that NE localization depends

117   on the Mto1 N-terminus interacting with exportin Crm1, a nuclear transport receptor, and

118   nucleoporin Nup146, a component of the nuclear pore complex (NPC). We further find that

119   although Mto1 is an exclusively cytoplasmic protein, it becomes stably docked at the NPC by

120   mimicking a nuclear export cargo. In addition to revealing the mechanism of MTOC

121   formation at the fission yeast NE, our work demonstrates a completely novel role for the

122   nuclear export machinery, in which the exportin is repurposed to create NPC-docking sites

123   for cytoplasmic proteins with functions unrelated to nuclear export.

124

125   **RESULTS**

126   ***MT nucleation from the NE contributes to nuclear positioning***

127   Mto1 localization to the NE is enhanced in the C-terminal truncation mutant

128   Mto1[NE], which lacks MASC and MT-localization domains ((Lynch et al., 2014); Fig. 1A).

129   Previously we deleted amino acids 1-130 from Mto1[NE] and from full-length Mto1 to make

130   Mto1[bonsai] and Mto1[Δ130], respectively (Fig. 1A), and we showed that these deletions

131   lead to loss of Mto1/2 complex from the NE, accompanied by loss of MT nucleation from the

132   NE (Lynch et al., 2014). However, in that work the consequences of this altered MT

133   nucleation were not investigated. In fission yeast, MT-dependent pushing forces are thought

134   to center the interphase nucleus precisely in the cell middle (Tran et al., 2001). Because

135   nuclear position during early mitosis determines the future cell division plane, this ensures

136   equal size of daughter cells after cell division (Daga & Chang, 2005). To investigate whether

137   MT nucleation from the NE contributes to nuclear positioning, we measured interphase

138   nuclear position in *mto1-GFP*, *mto1[NE]-GFP*, *mto1[Δ130-GFP]* and *mto1[bonsai]-GFP* cells

139   (Fig. 1A; Fig. 1 Suppl. 1A). (In these and all subsequent experiments, *mto1* mutants replace

140   endogenous wild-type *mto1+* at the *mto1* locus, and in this particular experiment, all versions

141   of *mto1* were GFP-tagged to equalize protein expression levels (Lynch et al., 2014)).

142   Interestingly, nuclear positioning was less accurate in *mto1[bonsai]-GFP* and *mto1[Δ130]-*

143   *GFP* cells compared to *mto1[NE]-GFP* and *mto1-GFP* cells, indicating that MT nucleation

144   from the NE contributes to nuclear positioning. By contrast, there was no difference in

145   nuclear positioning between wild-type and *mto1[NE] cells*, or between *mto1[131-1115]* and

146   *mto1[bonsai]* cells, indicating that MT nucleation from the SPB is not particularly important

147   for nuclear positioning.

148

149

150   ***Identification of proteins interacting with Mto1[NE] but not with Mto1[bonsai]***

151   To identify proteins involved in recruiting Mto1 to the NE, we wanted to compare

152   interactomes of Mto1[NE] vs. Mto1[bonsai]. Initially we attempted to use SILAC mass

153   spectrometry (MS) (Bicho et al., 2010, Ong et al., 2002) to compare anti-GFP

154   immunoprecipitates of Mto1[9A1-NE]-GFP and Mto1[9A1-bonsai]-GFP, which are otherwise

155   identical to Mto1[NE]-GFP and Mto1[bonsai]-GFP except for the additional mutation of nine

156   consecutive amino acids in the CM1 domain to alanine (Samejima et al., 2008), Fig 1A); the

157   *9A1* mutation disrupts interaction with the γ-tubulin complex and thereby enhances

158   localization of Mto1[NE] to the NE ((Lynch et al., 2014); Fig. 1 Suppl. 1B). In preliminary

159   experiments, however, we found that the immunoprecipitation approach yielded low peptide

160   counts for many Mto1-interactors of potential interest (Suppl. File 2). We therefore decided

161   to develop a more robust method to capture interactors even when they may be low-

162   abundance and/or low-affinity interactors.

163   We tagged Mto1[9A1-NE] and Mto1[9A1-bonsai] at their N-termini with GFP and at

164   their C-termini with an HTB (His-TEV-biotin) tag, which allows for two-step purification of a

165   tagged protein under fully denaturing conditions after cross-linking to interactors (Tagwerker

166   et al., 2006) (Fig. 1B). As expected, GFP-Mto1[9A1-NE]-HTB localized to the NE in vivo,

167   while GFP-Mto1[9A1-bonsai]-HTB was present only in the cytoplasm (Fig. 1C).

168   Disuccinimidyl suberate (DSS) cross-linking of cell cryogrindates shifted a significant

169   proportion of HTB-tagged Mto1 into higher molecular-weight species (Fig. 1D). After DSS

170   cross-linking and denaturing purification (Fig. 1E; see Materials and Methods), we analyzed

171   cross-linked adducts of GFP-Mto1[9A1-NE]-HTB and GFP-Mto1[9A1-bonsai]-HTB by label-

172   free quantification (LFQ) MS ((Cox & Mann, 2008, Tyanova et al., 2016); Fig. 1F; Fig. 1

173   Suppl. 1C; Suppl. File 3). Among the proteins significantly enriched in the Mto1[9A1-NE]

174   interactome vs. the Mto1[9A1-bonsai] interactome, we identified nucleoporin Nup146

175   (Asakawa et al., 2014, Chen et al., 2004), exportin Crm1 (Adachi & Yanagida, 1989, Fung &

176   Chook, 2014, Hutten & Kehlenbach, 2007, Stade et al., 1997), the fission yeast TACC

177   homolog, Alp7 (Sato et al., 2004), and, to a lesser extent, polo kinase Plo1 (Ohkura et al.,

178   1995).

179   Neither Alp7 nor Plo1 is known to localize to the NE, and Plo1 was not investigated

180   further. The interaction of Mto1[NE] with Alp7 was of potential interest because of the role of

181   Alp7 in microtubule organization (Ling et al., 2009, Sato et al., 2009, Zheng et al., 2006), and

182   an interaction between Mto1 and Alp7 has been confirmed independently (M. Sato, Waseda

183   University, personal communication, July 2017). However, we found that in *alp7Δ* deletion

184   mutants, Mto1[9A1-NE]-GFP was present on the NE just as in wild-type (*alp7+*) cells (Fig. 1

185   Suppl. 1D). This indicates that Alp7 is not required for Mto1 localization to the NE.

186

187 ***Mto1[NE] associates with the cytoplasmic face of the NPC***

188   The interaction of Mto1[9A1-NE] with Nup146 suggested that Mto1 may localize to

189 nuclear pore complexes (NPCs) on the NE. We therefore imaged Mto1[9A1-NE]-GFP

190 together with Nup146-3mCherry in a *nup132Δ* background, in which NPCs can become

191 clustered on the NE (Bai et al., 2004). We observed extensive colocalization of Mto1[9A1-

192 NE]-GFP with Nup146-3mCherry clusters (Fig. 2A), indicating specific association with

193 NPCs.

194   We also examined Mto1[9A1-NE]-GFP localization by immunoelectron microscopy.

195 Close homologs of Nup146 in budding yeast (Nup159; referred to here as *Sc* Nup159) and

196 humans (Nup214; referred to as *Hs* Nup214) are both located exclusively at the cytoplasmic

197 face of NPCs (Gorsch et al., 1995, Kraemer et al., 1994, Kraemer et al., 1995), and indirect

198 evidence suggests that this is also the case for Nup146 (Lo Presti et al., 2012). Consistent

199 with this, we observed Mto1[9A1-NE]-GFP specifically at the cytoplasmic face of NPCs (Fig.

200 2B).

201

202 ***Mto1 localization to NPCs requires export cargo-binding activity of exportin Crm1***

203   The interaction of Mto1[NE] with Crm1 was both surprising and puzzling. As the

204 major transport receptor for nuclear export of proteins (as well as some RNAs), Crm1

205 normally forms a trimeric complex with export cargo and RanGTP within the nucleus, which

206 facilitates transit of cargo through the permeability barrier of the NPC and into the cytoplasm

207 (Dong et al., 2009, Fung & Chook, 2014, Hutten & Kehlenbach, 2007). However, to date

208 there is no evidence that Mto1 is a nuclear export cargo or indeed is ever present in the

209 nucleus.

210   Because deletion of *crm1+* is lethal (Adachi & Yanagida, 1989), we investigated the

211 significance of the Mto1-Crm1 interaction by asking whether inhibition of Crm1 cargo-binding

212 activity affects Mto1 localization to NPCs. Nuclear export cargos typically bind to Crm1 via

213 hydrophobic nuclear export signals (NESs) (Dong et al., 2009, Fung & Chook, 2014, Fung et

214 al., 2015, Guttler et al., 2010, Hutten & Kehlenbach, 2007, Kutay & Guttinger, 2005). This

215 can be inhibited by the drug leptomycin B (LMB), which binds within the hydrophobic NES-

216 binding cleft of Crm1 ((Dong et al., 2009, Fornerod et al., 1997a, Fukuda et al., 1997, Fung

217 & Chook, 2014, Ossareh-Nazari et al., 1997). As a result, when cells are treated with LMB,

218 nuclear export cargos accumulate within the nucleus. Interestingly, after LMB treatment, we

219 found that Mto1[9A1-NE]-GFP was lost from NPCs (Fig. 3A). Strikingly, however, rather than

220 accumulating in the nucleus, Mto1[9A1-NE]-GFP became dispersed in the cytoplasm.

221   Given the unusual behavior of Mto1[9A1-NE]-GFP after LMB treatment, we

222 confirmed that LMB was inhibiting nuclear export. We assayed localization of Alp7, which

223 shuttles continuously in and out of the nucleus during interphase, in complex with its partner

224   protein Alp14 (ch-TOG homolog) (Okada & Sato, 2015, Okada et al., 2014)(Fig. 3 Suppl.

225   1A). In the absence of LMB, Alp7-3GFP was present in the cytoplasm, primarily as puncta

226   on cytoplasmic MTs. As expected, after LMB treatment, Alp7-3GFP accumulated in the

227   nucleoplasm and on the intranuclear MT bundle that forms upon LMB treatment of fission

228   yeast (Matsuyama et al., 2006)(Fig. 3 Suppl. 1A).

229   In addition, to rule out the possibility that loss of Mto1[9A1-NE]-GFP from NPCs was

230   due to an off-target effect of LMB (i.e., unrelated to Crm1 inhibition), we generated an LMB-

231   resistant *crm1* mutant. LMB is a particularly potent inhibitor of Crm1 because it reacts

232   covalently with cysteine 529 (C529) in Crm1's NES-binding cleft (Kudo et al., 1999). We

233   mutated C529 in the endogenous *crm1* coding sequence to alanine (*crm1-C529A*), as well

234   as to other amino acids (Fig. 3B, Fig. 3 Suppl. 1B,C). The *crm1-C529A* mutant was viable,

235   indicating that it preserves essential functions of *crm1* for nuclear export, and resistant to

236   high concentrations of LMB (Fig. 3 Suppl. 1B). Interestingly, we found that in *crm1-C529A*

237   cells, Mto1[9A1-NE]-GFP localized to NPCs both in the absence and in the presence of LMB

238   (Fig. 3B). This demonstrates that loss of Mto1 from NPCs after LMB treatment can be

239   specifically attributed to inhibition at the Crm1 cargo-binding cleft.

240

241   ***Mto1 interacts with Crm1 via a nuclear export signal-like sequence***

242   How might Crm1 cargo-binding activity be involved in Mto1 localization to the NPC?

243   We hypothesized that Mto1 itself might bind to Crm1 as an unconventional "cargo" and

244   somehow exploit this interaction to localize to the cytoplasmic face of the NPC. To test this,

245   we used LFQ MS to compare GFP-Mto1[9A-NE]-HTB interactomes prepared from untreated

246   vs. LMB-treated cells (Fig 3C; Fig. 3 Suppl. 1D; Suppl. File 4). Interestingly, only 3-4 out of

247   nearly 500 quantified proteins were significantly enriched in the GFP-Mto1[9A1-NE]-HTB

248   interactome from untreated cells compared to LMB-treated cells. Among these, Crm1

249   showed the greatest enrichment (~20X). Nup146 also showed enrichment, but to a lesser

250   extent (~2.8X), which may indicate that Mto1 can bind weakly to Nup146 independently of

251   Crm1 (see Discussion). These results demonstrate that, like Mto1 localization to NPCs,

252   Mto1 interaction with Crm1 requires Crm1 cargo-binding activity.

253   Based on these findings, we next used the LocNES algorithm (Xu et al., 2015) to

254   search for NES-like sequences within the N-terminal 130 amino acids of Mto1, which are

255   present in Mto1[NE] but absent from Mto1[bonsai]. The sequence spanning Mto1 amino

256   acids 9-25 contained two closely overlapping candidate NESs (Fig. 4A). Interestingly, the

257   spacing of hydrophobic amino acids within this NES-like sequence is similar to that of

258   several non-natural high-affinity NESs (Fig. 4B; (Engelsma et al., 2004, Guttler et al., 2010)).

259   To investigate the role of the Mto1 NES-like sequence, we deleted the first 25 amino

260   acids of Mto1 from GFP-Mto1[9A1-NE]-HTB. The truncated protein, termed GFP-

261   Mto1[ΔNES-9A1-NE]-HTB, failed to localize to NPCs and instead was present in the

262   cytoplasm (Fig. 4C). In parallel, we used LFQ MS to determine how the ΔNES truncation

263   affected the GFP-Mto1[9A1-NE]-HTB interactome. As with LMB treatment, very few proteins

264   were enriched in the GFP-Mto1[9A1-NE]-HTB interactome compared to GFP-Mto1[ΔNES-

265   9A1-NE]-HTB interactome (Fig. 4D; Fig. 4 Suppl. 1; Suppl. File 5). However, we observed

266   strong enrichment of both Crm1 (~85X) and Nup146 (~20X). The importance of the Mto1

267   NES-like sequence both for localization to NPCs and for interaction with Crm1 strongly

268   suggests that Mto1 is a direct but unconventional cargo for Crm1. Because of the unusual

269   role of the Mto1 NES-like sequence, we will refer to it as a "NES-mimic" (NES-M).

270

271   ***The Mto1 NES-mimic is sufficient for nuclear envelope localization***

272   We next asked whether the Mto1 NES-M is sufficient to localize a reporter protein to

273   the NPC. We replaced endogenous Mto1 with GFP-Mto1[1-29]-GST, which contains only

274   the first 29 amino acids of Mto1. Strikingly, GFP-Mto1[1-29]-GST localized to puncta on the

275   NE, which we interpret to be NPCs (Fig.4E). By contrast, GFP-Mto1[1-12]-GST, which lacks

276   the NES-M, did not show any specific localization. We further found that after LMB

277   treatment, GFP-Mto1[1-29]-GST was lost from NPCs (Fig. 4F); moreover, like Mto1[9A1-

278   NE]-GFP, GFP-Mto1[1-29]-GST was present exclusively in the cytoplasm after LMB

279   treatment.

280   Compared to GFP fusions with Mto1[NE], GFP-Mto1[1-29]-GST had a weaker

281   punctate localization at NPCs. We hypothesized that this may be due an avidity effect,

282   because Mto1[NE] can form higher-order multimers, via its coiled-coil region and via

283   interaction with Mto2 (Lynch et al., 2014), whereas GFP-Mto1[1-29]-GST would be expected

284   to form only dimers, via the GST domain. To investigate whether dimerization may

285   contribute to NPC localization, we analyzed localization of a GFP-Mto1[1-29]-13Myc fusion

286   protein, which should be monomeric. GFP-Mto1[1-29]-13Myc did not localize to NPCs (Fig.

287   4E), suggesting that dimerization/multimerization may be an important factor for Mto1 NPC

288   localization.

289   Collectively, these results indicate the Mto1 NES-M is both necessary and sufficient

290   for localization to NPCs, without ever being present in the nucleus.

291

292   ***Mto1 NPC localization requires RanGTP***

293   To further investigate similarities between the mechanism of Mto1 localization to

294   NPCs and nuclear export, we tested whether Mto1 localization depends on the nucleotide

295   state of Ran. Net directional transport of conventional cargos through the NPC depends on a

296   RanGTP gradient across the NE, generated by Ran GTPase activating protein (RanGAP) in

297   the cytoplasm and Ran guanine-nucleotide exchange factor (RanGEF) in the nucleus

298 (Aitchison & Rout, 2012, Gorlich & Kutay, 1999, Wente & Rout, 2010). Importins bind import

299 cargos in the cytoplasm, where RanGTP concentration is low, and release them in the

300 nucleus, where RanGTP concentration is high. By contrast, exportins bind cooperatively to

301 export cargos and RanGTP within the nucleus to form trimeric export complexes, which then

302 dissociate after export, accompanied by RanGTP hydrolysis aided by RanGAP (Fornerod et

303 al., 1997a, Fung & Chook, 2014, Guttler & Gorlich, 2011, Koyama & Matsuura, 2012,

304 Monecke et al., 2014). The role of Ran can be addressed by expressing mutant versions of

305 Ran (encoded by the *spi1+* gene in fission yeast; (Matsumoto & Beach, 1991)) that mimic

306 either GTP or GDP states (Bischoff et al., 1994, Klebe et al., 1995). Constitutively-active

307 Ran (RanQ69L in humans) is defective in GTP hydrolysis and thus "locked" in the RanGTP

308 state, while inactive/dominant-negative Ran (RanT24N in humans) has low affinity for

309 nucleotide and competes with endogenous RanGDP for binding to RanGEF.

310 We expressed wild-type *spi1+*, *spi1[Q68L]* (equivalent to human RanQ69L), and

311 *spi1[T23N]* (equivalent to human RanT24N) as integrated transgenes from a thiamine-

312 repressible promoter. All cells were viable under repressing conditions, but growth was

313 impaired by expression of *spi1[Q68L]* or *spi1[T23N]* (Fig. 5 Suppl. 1A), consistent with

314 phenotypes of the equivalent mutants in vertebrate cells (Clarke et al., 1995, Dasso et al.,

315 1994, Kornbluth et al., 1994, Ren et al., 1994). To avoid any indirect effects on Mto1[9A1-

316 NE]-GFP localization as a result of growth impairment, we assayed localization as early as

317 possible during expression (Fig. 5, Fig. 5 Suppl. 1B). Expression of *spi1+* had no effect on

318 Mto1[9A1-NE]-GFP localization. Expression of *spi1[Q68L]* impaired import of a nuclear

319 localization signal (NLS) reporter protein, as expected (Fig. 5 Suppl. 1B), but did not alter

320 Mto1[9A1-NE]-GFP localization to NPCs. Interestingly, expression of *spi1[T23N]*, which had

321 only minor effects on NLS reporter localization, led to strong loss of Mto1[9A1-NE]-GFP from

322 NPCs (Fig. 5, Fig. 5 Suppl. 1B). These results indicate that, like nuclear export, Mto1

323 localization to NPCs requires RanGTP. Moreover, at least in the short-term, neither

324 RanGDP nor Ran nucleotide cycling is required for Mto1 NPC localization.

325

326 ***Mto1-Crm1 complex docks at the NPC via Nup146 FG repeats.***

327 We next asked whether Nup146 contributes to Mto1 NPC localization. Like

328 approximately one-third of all nucleoporins, Nup146 and its homologs *Sc* Nup159 and *Hs*

329 Nup214 contain multiple phenylalanine-glycine (FG) repeats, which bind directly to importins

330 and/or exportins (Fig. 6 Suppl. 1A; (Aitchison & Rout, 2012, Wente & Rout, 2010)). Because

331 of their location on the cytoplasmic face of the NPC, these nucleoporins are classified as

332 "cytoplasmic FG-Nups", distinguishing them from the "symmetric FG-Nups" present within

333 the central permeability barrier of the NPC. While FG repeats of symmetric FG-Nups directly

334 facilitate cargo transport through the NPC, FG repeats of cytoplasmic FG-Nups are thought

335 not to be important for transport *per se* (Adams et al., 2014, Strawn et al., 2004, Zeitler &

336 Weis, 2004), although their other (non-FG) regions recruit proteins for processes linked to

337 transport (e.g. mRNP processing after export (Napetschnig et al., 2007, Schmitt et al., 1999,

338 Weirich et al., 2004); Fig. 6 Suppl. 1A). Nevertheless, the FG repeats of *Sc* Nup159 and *Hs*

339 Nup214 have been shown to bind to Crm1 with high specificity relative to other

340 importins/exportins. (Allen et al., 2002, Fornerod et al., 1997b, Hutten & Kehlenbach, 2006,

341 Port et al., 2015, Roloff et al., 2013, Zeitler & Weis, 2004). We therefore focused attention on

342 the Nup146 FG repeats.

343   We deleted the 50-amino-acid region comprising FG repeats 5-12 (out of a total of 16

344 FG repeats) from the endogenous *nup146* coding sequence (Fig. 6A). Although complete

345 deletion of *nup146* is lethal (Chen et al., 2004), the *nup146[ΔFG5-12]* strain was viable, and

346 Nup146[ΔFG5-12]-3mCherry was localized to NPCs. (Fig. 6 Suppl. 1B). Strikingly, in

347 *nup146[ΔFG5-12]* cells, Mto1[9A1-NE]-GFP no longer localized to NPCs and instead was

348 present only in the cytoplasm (Fig. 6B; Fig. 6 Suppl. 1B).

349   We also analyzed MTOC activity at the NE in wild-type (*nup146+*) cells vs. *nup146*

350 *[ΔFG5-12]* cells. We used immunofluorescence to assay MT regrowth after cold-shock, in

351 cells expressing full-length Mto1 (Fig. 6C). In wild-type cells, cold-induced MT

352 depolymerization causes the pool of Mto1 normally associated with the cytoplasmic MTs to

353 redistribute to the NE; as a result, when cells are rewarmed, nearly all MT nucleation

354 initiates from the NE (Sawin et al., 2004). By contrast, we found that during MT regrowth in

355 *nup146[ΔFG5-12]* cells, MTs were nucleated randomly in the cytoplasm (Fig. 6C).

356   In addition, we used live-cell imaging of GFP-tubulin to assay steady-state MT

357 nucleation in cells expressing Mto1[NE]-GFP (Fig. 6D, E; in these cells, Mto1[NE]-GFP is

358 too faint to be seen relative to GFP-tubulin). In *nup146[ΔFG 5-12]* cells, MT nucleation

359 frequency in the vicinity of the NE was decreased by ~90% relative to wild-type (*nup146+*)

360 cells, while nucleation frequency away from the NE was unchanged.

361   Collectively, these results indicate that Nup146 FG repeats 5-12 are essential for

362 Mto1 docking at the NPC and, consequently, for MTOC nucleation from the NE. To our

363 knowledge, this is the first biological function that can be uniquely attributed to the FG

364 repeats of the Nup146/*Sc* Nup159/*Hs* Nup214 class of cytoplasmic FG-Nups, in any

365 organism (see Discussion).

366

367 ***Nup146 FG repeats stabilize the Mto1-Crm1 interaction***

368   Our results thus far indicate that a RanGTP-dependent Mto1-Crm1 "cargo-like"

369 complex docks at the cytoplasmic face of the NPC via a mechanism involving Nup146 FG

370 repeats (see Fig. 7). Interestingly, a subset of FG repeats in *Hs* Nup214 have been shown to

371 bind to Crm1 in a manner that stabilizes the Crm1-RanGTP-cargo interaction *in vitro*

372   (Askjaer et al., 1999, Fornerod et al., 1997b, Hutten & Kehlenbach, 2006, Kehlenbach et al.,

373   1999, Port et al., 2015, Roloff et al., 2013). We therefore asked whether Nup146 FG repeats

374   5-12 are important for Mto1 interaction with Nup146, and whether these repeats contribute

375   to Crm1 association with Mto1 *in vivo*. We used LFQ MS to compare GFP-Mto1[9A1-NE]-

376   HTB interactomes from wild-type (*nup146+*) vs. *nup146[ΔFG5-12]* cells. Among more than

377   500 quantified proteins, only 5-6 proteins were significantly enriched in the GFP-Mto1[9A1-

378   NE]-HTB interactome from *nup146+* cells compared to *nup146[ΔFG5-12]* cells. Nup146 itself

379   showed the greatest enrichment (~11X), while Crm1 was also enriched, although to a lesser

380   extent (~3X) (Fig. 6F; Fig. 6 Suppl. 1C; Suppl. File 6). This suggests that Nup146 FG

381   repeats are essential for interaction of Mto1 with Nup146. In addition, while Nup146 FG

382   repeats may not be absolutely essential for formation of an Mto1-Crm1 complex, they may

383   help to stabilize it.

384

385   **DISCUSSION**

386   While different mechanisms are involved in generating non-centrosomal MTOCs at

387   different subcellular sites, at many sites the mechanisms themselves remain poorly

388   understood (Petry & Vale, 2015, Sanchez & Feldman, 2017, Wu & Akhmanova, 2017). Here

389   we have shown how MTOCs are generated at the NE in fission yeast *S. pombe* via the

390   Mto1/2 complex. We find that Mto1 docks at the cytoplasmic face of NPCs, through a novel

391   mechanism in which the nuclear export machinery is repurposed for a non-export-related

392   function. Docking depends on an export cargo-like interaction between a NES-like sequence

393   (NES-M) at the Mto1 N-terminus and the NES-binding cleft of exportin Crm1, the major

394   transport receptor for protein nuclear export (Fung & Chook, 2014, Hutten & Kehlenbach,

395   2007, Kutay & Guttinger, 2005). Docking further requires RanGTP and the central FG

396   repeats of Nup146, a cytoplasmic FG-Nup homologous to *Sc* Nup159 and *Hs* Nup214. The

397   general features of Mto1 docking at NPCs are summarized in Fig. 7.

398   In this work, chemical cross-linking of cell cryogrindates allowed us to capture low-

399   affinity interactions that might otherwise be unstable during conventional purification. By

400   using affinity tags compatible with strong denaturing conditions (Tagwerker et al., 2006), we

401   were able to solubilize and interrogate protein-protein interactions that normally occur within

402   "solid-phase" subcellular environments. In addition, by combining live-cell microscopy with

403   LFQ MS (Cox & Mann, 2008) we were able to correlate changes in Mto1 localization with

404   changes in interactors on a near proteome-wide scale, and under several different

405   comparative conditions.

406   The mechanism described here for Mto1 localization to NPCs was entirely

407   unexpected. While it incorporates many of the elements of conventional Crm1-dependent

408   nuclear export (Fig. 7), there are two fundamental distinctions. First, when not interacting

409   with the export machinery, Mto1(and its partner Mto2) is a cytoplasmic protein rather than a

410   nuclear protein. Second, interaction of Mto1 with the export machinery leads to docking at

411   NPCs, rather than a return/release into the cytoplasm. Previously, nuclear transport

412   receptors such as importins and Crm1 have been shown to function away from NPCs in

413   non-transport-related roles, including regulation of mitotic spindle assembly factors

414   (reviewed in (Cavazza & Vernos, 2015, Forbes et al., 2015, Kalab & Heald, 2008)), targeting

415   of the Ran pathway to kinetochores (Arnaoutov et al., 2005), and tethering the Chromosome

416   Passenger Complex to centromeric chromatin (Knauer et al., 2006). However, to our

417   knowledge, this is the first example of a nuclear export-like complex being used to dock a

418   cytoplasmic "cargo" at the NPC, with no obvious functional link to export. This in turn raises

419   questions as to how such a complex could be formed, and how it becomes docked.

420

421   ***Docking at the NPC***

422   How does Mto1, a nuclear export cargo "mimic", become docked at the NPC, while

423   conventional export cargos are released into the cytoplasm? Ultimately, a detailed

424   understanding of this issue will require *in vitro* biochemistry with purified proteins. However,

425   based on previous work in mammalian cells (Engelsma et al., 2004, Port et al., 2015), we

426   speculate that docking may depend on: 1) the Mto1 NES-M acting as a high-affinity NES;

427   and 2) the stability of interaction between Mto1-Crm1 and Nup146 FG repeats.

428   The Mto1 NES-M is necessary and sufficient for docking at the NPC (Fig. 4).

429   Interestingly, in human cells, cargo containing a non-natural, high-affinity NES (a

430   "supraphysiological NES") was shown to accumulate at the cytoplasmic face of the NPC and

431   also to enhance Crm1 accumulation at the same site (Engelsma et al., 2004, Engelsma et

432   al., 2008). We hypothesize that the Mto1 NES-M may be a *natural* high-affinity NES. In

433   recent years, the NES "consensus" has evolved in concert with new experimental findings

434   (Dong et al., 2009, Fung et al., 2015, Fung et al., 2017, Guttler et al., 2010, Monecke et al.,

435   2009). In particular, relative to an original consensus involving four spaced hydrophobic

436   residues (Kutay & Guttinger, 2005), several high-affinity NESs depend on a fifth hydrophobic

437   residue, which may also be present in the Mto1 NES-M (Fig. 4B). We also note that

438   Mto1[9A1-NE]-GFP localizes to NPCs in *crm1-C529A* mutants (Fig. 3B) but fails to localize

439   to NPCs in *crm1-C529S, crm1-C529T, and crm1-C529V* mutants, even though these

440   mutants are viable and thus competent for nuclear export (Fig. 3 Suppl. 1B, C). This may

441   indicate that, relative to conventional NESs, the binding of the Mto1 NES-M to Crm1 involves

442   recognition of additional features within the Crm1 NES-binding cleft.

443   Assuming that the Mto1 NES-M interacts with Crm1 as a high-affinity NES, clues as

444   to how this could lead to accumulation at the NPC can be found in structural studies of Crm1

445   alone and Crm1 in complex with RanGTP, cargo, and an FG-repeat fragment of *Hs* Nup214

446 (Fig. 7 Suppl. 1A; (Dong et al., 2009, Guttler et al., 2010, Monecke et al., 2009, Monecke et

447 al., 2013, Port et al., 2015, Saito & Matsuura, 2013)). Crm1 can exist in two conformations:

448 an unliganded extended, superhelical conformation, which is inhibitory to cargo and

449 RanGTP binding, and a compact, ring-like conformation, which is stabilized by cooperative

450 binding to cargo and RanGTP. Importantly, the FG-repeat fragment of *Hs* Nup214, which

451 binds Crm1 cooperatively with RanGTP and cargo, interacts with the compact conformation

452 of Crm1 at multiple sites, spanning the junction between the Crm1 N- and C-termini in a

453 manner similar to an adhesive bandage (Port et al., 2015) (Fig. 7 Suppl. 1A). The *Hs*

454 Nup214 FG repeats have therefore been described as a "molecular clamp" that can stabilize

455 Crm1-RanGTP-cargo complex in the compact conformation (Port et al., 2015). However,

456 from an energetic perspective, cooperative binding also implies that anything that stabilizes

457 the Crm1 compact conformation (including a high-affinity NES) will correspondingly reinforce

458 association of Crm1 with *Hs* Nup214 FG repeats. As a result, a sufficiently high-affinity NES

459 cargo would be expected to stabilize interaction of Crm1 with Nup146, leading to docking of

460 Crm1 (and the NES cargo itself) at the cytoplasmic face of the NPC (Fig. 7 Suppl. 1A).

461 In addition to a "high-affinity NES" mechanism, other factors may also contribute to

462 docking of the Mto1/2 complex at the NPC. For example, if Mto1(or its partner Mto2) were to

463 bind Nup146 independently of binding to Crm1, such multivalent binding would decrease the

464 off-rate from the NPC; currently our MS data cannot distinguish between direct and indirect

465 Mto1 interactors. Interactions between Mto1/2 and the NPC could also be stabilized by

466 avidity effects. Mto1/2 is multimeric *in vivo*, containing multiple (>10) copies of both Mto1

467 and Mto2 (Lynch et al., 2014), while nucleoporins are also present in multiple copies within

468 the NPC, because of its eight-fold symmetry (Aitchison & Rout, 2012, Gorlich & Kutay, 1999,

469 Wente & Rout, 2010). As a result, multiple Mto1 molecules in a single Mto1/2 complex could

470 bind to multiple nucleoporins (and/or Crm1) in a single NPC. Interestingly, localization of

471 Mto1/2 to the SPB and the CAR also depends on avidity effects (Samejima et al., 2010).

472

473 ***Formation of an Crm1-dependent docking complex with a cytoplasmic "cargo"***

474 Given that conventional Crm1-dependent export complexes form in the nucleus,

475 where RanGTP concentration is high (Aitchison & Rout, 2012, Gorlich & Kutay, 1999, Wente

476 & Rout, 2010), how might an Mto1/2 docking complex form in the cytoplasm, where RanGTP

477 concentration is low? We speculate that if the Mto1 NES-M acts as a high-affinity NES, it

478 may be possible for Mto1/2 to replace a conventional nuclear export cargo at the final stages

479 of export, via a "cargo-handover" mechanism (Fig. 7 Suppl. 1B). Alternatively, a docking

480 complex involving Mto1/2, Crm1, Nup146 and RanGTP could in principle form *de novo* at

481 the cytoplasmic face of the NPC. While the low concentration of RanGTP in the cytoplasm

482 makes this unlikely, it is formally possible that in the immediate vicinity of the NPC, the local

483   concentration of RanGTP is higher than in the cytoplasm in general, because in yeast,

484   RanGAP is freely soluble in the cytoplasm rather than associated with the NPC (Aitchison &

485   Rout, 2012, Hopper et al., 1990). Accordingly, immediately after RanGTP dissociates from

486   export complexes (but prior to GTP hydrolysis), it might be available to cytoplasmic Mto1/2.

487

488   *A novel function for cytoplasmic FG-Nups?*

489   In this work, we identified a very specific phenotype associated with deletion of

490   Nup146 FG repeats 5-12: Mto1 is lost from NPCs, with a concomitant loss in MT nucleation

491   from the NE. Moreover, this is correlated with a strong decrease in interaction of Mto1 with

492   Nup146 and, to a lesser extent, with Crm1, consistent with our model of a cargo-like

493   complex of Mto1/2, Crm1 and RanGTP docking at the cytoplasmic face of the NPC. In this

494   context, it is interesting that extensive analysis in budding yeast has shown that the FG

495   regions of cytoplasmic FG-Nups (as well as nucleoplasmic FG-Nups) can be deleted without

496   almost any discernible effects on nuclear transport (Adams et al., 2014, Strawn et al., 2004,

497   Zeitler & Weis, 2004). In human cells, the role of *Hs* Nup214 in protein export appears to be

498   somewhat controversial (Bernad et al., 2006, Hutten & Kehlenbach, 2006); however, similar

499   to budding yeast, in at least one instance where *Hs* Nup214 was found to be important for

500   export—namely, export of the 60S pre-ribosome— the FG repeats of *Hs* Nup214 were found

501   not to be required (Bernad et al., 2006)). Based on these results, and on the conservation of

502   FG repeats in Nup146, *Sc* Nup159 and *Hs* Nup214, we propose that an important but

503   previously unrecognized role for cytoplasmic FG-Nups may be to dock cytoplasmic proteins

504   at the NPC for non-export-related functions, as described here for generation of non-

505   centrosomal MTOCs by the Mto1/2 complex. It will be interesting to see how widespread this

506   type of repurposing of the nuclear export machinery is in eukaryotic cells more generally.

507

508

509   **MATERIALS AND METHODS**

510   **Yeast cultures, strain and plasmid construction**

511   Fission yeast methods and growth media were as described (Forsburg & Rhind,

512   2006, Petersen & Russell, 2016). Strains were normally grown in YE5S rich medium or PMG

513   minimal medium (like EMM2, but using 5 g/L sodium glutamate acid instead of ammonium

514   chloride as nitrogen source). For preliminary experiments using SILAC mass spectrometry,

515   cells were grown in low-nitrogen EMM2 medium ("LowN"; using 0.3 g/L ammonium chloride

516   as nitrogen source; (Bicho et al., 2010)). For purification of HTB-tagged Mto1 variants for

517   LFQ MS, Mto1 variants were expressed from the *nmt81* promoter, and cells were grown in

518   PMG medium, except for experiments involving leptomycin B (Fig. 3), in which case Mto1

519   variants were expressed from the repressed *nmt1* promoter, and cells were grown in

520   4xYE5S medium. For electron microscopy, cells were grown in EMM2 minimal medium.

521   Nutritional supplements were normally used at 175 mg/L, except for arginine and lysine in

522   SILAC experiments, in which unlabeled arginine or L-^{13}C$_6$-arginine (Sigma Isotec) was

523   used at 80 mg/L, and unlabeled lysine or L-^{13}C$_6$^{15}N$_2$-lysine (Sigma Isotec) was used at 60

524   mg/L (Bicho et al., 2010). Solid media contained 2% Bacto agar (Becton Dickinson). For

525   mating, SPA plates containing 45 mg/L each of adenine, leucine, uracil, histidine and lysine

526   were used. For repression of thiamine-regulated promoters, sterile-filtered thiamine was

527   added to media at a final concentration of 15 μM.

528   Strains used in this study are listed in Supplementary File 1. For experiments

529   purifying HTB-tagged Mto1 for LFQ MS, strains contained the *mto2[17A]* allele; this allele

530   contains 17 phosphorylation sites in Mto2 mutated to alanine, which helps to stabilize the

531   Mto1/2 complex (Borek et al., 2015). The *mto2[17A]* allele was also present in strains

532   imaged in Figs. 1C and 4C (see Supplementary File 1).

533   Genetic crosses used either tetrad dissection or random spore analysis (Ekwall &

534   Thon, 2017). Except for the cases described below, genome manipulations such as gene

535   tagging, truncation and/or deletion were made by homologous recombination of PCR

536   products (Bahler et al., 1998). PCR was performed with either Phusion High-Fidelity

537   polymerase or Q5 High-Fidelity polymerase (NEB). Desired strains were confirmed by yeast

538   colony PCR, western blot and/or fluorescence microscopy as appropriate. For all cloning

539   experiments, *E. coli* strain DH5alpha was used.

540

Leptomycin-resistant crm1 mutants

542   To generate *crm1-C529A/S/T/V* mutants, a one-step approach was used, in which

543   *mto1[9A1-NE]-GFP nup146-3mCherry* cells were transformed with mutated *crm1* DNA

544   fragments and selected directly for leptomycin (LMB) resistance. Mutant *crm1* fragments

545   were designed with the mutation site in the center, ~650 base pairs of *crm1* sequence on

546   either side of the mutation site, and BstXI sites at each end of fragment. Plasmids

547   containing the mutant fragments were synthesized by GeneArt. The *crm1* fragments were

548   released from plasmids by BstXI digestion, purified and transformed into strain KS7255.

549   Cells from the transformation were plated onto YE5S plates containing 300 nM LMB (LC

550   Laboratories), and LMB-resistant colonies were easily identified. A negative-control

551   transformation conducted in parallel did not yield any LMB-resistant colonies. Stable LMB-

552   resistant colonies from each transformation were then used for sequencing to confirm

553   specific mutations in crm1 genomic DNA. The mutant strains were named KS9340 (*crm1-*

554   *C529A*), KS9221 (*crm1-C529S*) KS9338 (*crm1-C529T*), and KS9336 (*crm1-C529V*)

555

Overexpression of wild-type and mutant spi1

556

557　　　　Strains overexpressing *spi1+, spi1[Q68L]* and *spi1[T23N]* from the *nmt41* promoter

558 were generated by targeted integration of transgenes at the *hph.171k* locus (Fennessy et al.,

559 2014). First, pJET-spi1*+/[Q68L]/[T23N]* plasmids were constructed. To construct pJET-

560 *spi1+*, *spi1+* genomic DNA was amplified from fission yeast genomic DNA using primer pair

561 OKS3290/OKS3291, and the PCR product was ligated into vector pJET1.2 (Thermo Fisher

562 Scientific). The resulting pJET-*spi1+* plasmid was confirmed by sequencing and named

563 pKS1603. To construct pJET-spi1*[Q68L],* the *Q68L* mutation was introduced into pKS1603

564 by PCR, using primer pair OKS3139/OKS3140. The PCR product was recircularized using

565 T4 polynucleotide kinase and T4 DNA ligase. The resulting plasmid was confirmed by

566 sequencing and named pKS1596. To construct pJET-*spi1[T23N]*, pKS1603 was used as

567 template to introduce the *T23N* mutation into the *spi1* sequence, using QuikChange Site-

568 Directed Mutagenesis kit (Promega) and primer pair OKS 3336/OKS3337. After DpnI

569 treatment and transformation, the resulting plasmid was confirmed by sequencing and

570 named pKS1595.

571　　　　Next, the *spi1* inserts from pKS1603, pKS1596, and pKS1595 were each subcloned

572 into the fission yeast integration vector pINTH41 (Fennessy et al., 2014) after restriction

573 digest with BamHI and NdeI. The resulting pINTH41-*spi1+/[Q68L]/[T23N]* plasmids were

574 confirmed by restriction digest and named pKS1597, pKS1599, and pKS1598, respectively.

575　　　　For transformation into fission yeast, pKS1597, pKS1599, and pKS1598 were

576 digested with NotI, and the relevant fragments were purified and used to transform strain KS

577 7742. Stable nourseothricin-resistant, hygromycin-sensitive integrants were identified,

578 indicating replacement of the hygromycin-resistance marker at the *hph.171k* locus by the

579 transgene. Colonies were then tested on PMG plates (also containing adenine and uracil)

580 with or without 15 μM thiamine. After two days of growth at 32°C, *nmt41:spi1+* colonies were

581 similar with and without thiamine, while *nmt41:spi1[Q68L]* and *nmt41:spi1[T23N]* colonies

582 appeared normal on plates with thiamine but formed only very tiny colonies on plates without

583 thiamine. *nmt41: spi1+/[Q68L]/[T23N]* overexpression strains were named KS8578, KS8581

584 and KS8580, respectively.

585

Internal deletion of nup146 FG repeats

586

587　　　　Strains with internal deletions of *nup146* FG repeats were constructed by a two-step

588 approach (Fennessy et al., 2014). For the first step, an *rpl42:natMX6* cassette was amplified

589 by PCR using primer pair OKS2460/OKS2461 and the PCR product was used to transform

590 cycloheximide-resistant *rpl42.sP56Q* strain KS8072. The amplified cassette was at the end

591 of the *nup146* coding sequence to generate a nourseothricin-resistant, cycloheximide-

592 sensitive *nup146:rpl42:natMX6 rpl42.sP56Q* strain, which was named KS8254.

593   For the second step, a 5.1 kb wild-type *nup146* genomic DNA fragment (containing 5'

594   and 3' untranslated regions as well as coding sequence) was amplified by PCR using primer

595   pair OKS3063/OKS3067. The PCR product was ligated into pJET1.2 vector, and the

596   resulting pJET-*nup146* plasmid was sequenced and named pKS1511. Internal deletions of

597   FG repeats were made within pKS1511 by PCR, using primer pair OKS3093/OKS3094 to

598   make *nup146 [ΔFG5-12Δ]*. The PCR product was recircularized using T4 polynucleotide

599   kinase and T4 DNA ligase, and after transformation, the resulting plasmid was confirmed by

600   sequencing. The pJET-*nup146[ΔFG5-12]* genomic DNA plasmid was named pKS1514.

601   DNA sequence of *nup146 [ΔFG5-12]* was amplified from pKS1514 by PCR using

602   primer pair OKS3098/OKS3099. The resulting PCR product was transformed into strain

603   KS8254. Nourseothricin-sensitive, cycloheximide-resistant colonies were selected, and

604   colony PCR using primer pair OKS3154/OKS3155 was used to identify the desired strains.

605   The correct *nup146[ΔFG5-12] rpl42.sP56Q* strains was named KS8305.

606

607   **Light microscopy**

608   ***General light microscopy conditions***

609   Unless stated otherwise, for live-cell microscopy, cells were grown in PMG medium

610   supplemented with adenine, leucine and uracil, with glucose added after autoclaving. Before

611   imaging, cells were grown for two days at 25°C, with appropriate dilution to maintain

612   exponential growth. To prepare cells for imaging, 0.5-1 mL of cell culture was centrifuged at

613   13,000 rpm for 30 s to pellet cells, and a small amount of cell pellet was placed on a pad of

614   2% agarose in PMG medium supplemented with adenine, leucine and uracil, on a

615   microscope slide. The preparation was then sealed with a coverslip and VALAP (Vaseline,

616   lanolin, and paraffin wax in a 1:1:1 ratio). Preparations were used for ~10-40 min before

617   being discarded.

618   All microscopy was performed on a spinning-disk confocal microscope, using a Nikon

619   100x/1.45 NA Plan Apo objective and a Nikon TE2000 inverted microscope in a 25°C

620   temperature-controlled box, attached to a Yokogawa CSU-10 spinning disk confocal unit

621   (Visitech) and an Andor iXon+ Du888 EMCCD camera.

622   Images were acquired with a step size 0.6 μm and 11 Z-sections for the full cell

623   volume, except for imaging of GFP-tubulin, which used 7 Z-sections. Microscopy images

624   were processed and analyzed by Metamorph (Molecular Devices) and Image J software.

625   Only linear contrast enhancement was used. Unless otherwise indicated, images are

626   presented as maximum projection of all 11 Z-sections. Images within the same panel in a

627   given figure were all acquired and processed under identical conditions, and therefore signal

628   intensities can be compared directly.

629

LMB treatment

630

631   For imaging after LMB treatment. LMB (from 10 µM stock in ethanol) was added to

632   cultures at 100 nM final concentration. For negative controls, ethanol alone was added to an

633   equivalent final concentration (1% v/v). After incubation with or without LMB at 25°C, cells

634   were mounted on medium-agarose pads containing 100 nM LMB and imaged as described

635   above.

636

Spi1 expression

637

638   For imaging after expression of *nmt41:spi1+*, *nmt41:spi1[Q68L]*, and

639   *nmt41:spi1[T23N]*, cells were first grown to exponential phase in PMG medium containing

640   adenine, leucine and uracil, plus 15 µM thiamine to repress *nmt41:spi1* expression. Cells of

641   each strain, as well as control cells lacking any *spi1* transgene, were centrifuged at 4000

642   rpm for 4 min, washed three times with deionized water, resuspended in medium without

643   thiamine, and grown at 25°C until imaging. Preliminary experiments indicated that at this

644   temperature, expression was first noticeable ~26 h after washing, and more significant at 30-

645   34 h after washing. Cells were therefore imaged after 26 h and 34 h incubation at 25°C.

646

Microtubule re-growth after cold-shock

647

648   For microtubule regrowth experiments, cells were grown in YE5S liquid medium at

649   25°C. Manipulations before and after cold-shock, including methanol fixation and processing

650   for immunofluorescence, were performed exactly as described previously (Lynch et al.,

651   2014). To assay regrowth after cold-shock, chilled cells were fixed at 34 s, 40 s, 55 s, 70 s, 3

652   min, and 10 min after being returned to pre-warmed flasks in a 25°C water bath. Cells were

653   stained with TAT1 mouse monoclonal anti-tubulin antibody (1:15 dilution of hybridoma

654   culture supernatant) and Alexa488 Donkey anti-mouse secondary antibody (1:80 dilution;

655   Thermo Fisher Scientific). Centrifugation of stained cells onto coverslips for imaging was as

656   described (Sawin & Nurse, 1998).

657

GFP-tubulin live-cell imaging.

658

659   For GFP-tubulin live-cell imaging of wild-type (*nup146+*) and *nup146[ΔFG5-12]* cells,

660   cells were imaged every 5 s for a total time of 100s. Quantification of MT nucleation in the

661   vicinity of the cell nucleus and away from the cell nucleus was determined manually from

662   videos. 90 cells were scored for each of the two genotypes.

663

Immunoelectron microscopy

664

665   Immunoelectron microscopy was carried out as described previously (Tange et al.,

666   2016), with some modifications. Briefly, strain KS5750 (*mto1[9A1-NE]-GFP)* was cultured in

667   EMM2 medium with supplements. After washing with 0.1 M phosphate buffer (PB, pH7.4),

668   cells were fixed for 20 min at room temperature with 4% formaldehyde and 0.01%

669   glutaraldehyde dissolved in PB, and washed with PB three times for 5 min each. Cells were

670   then treated with 0.5 mg/mL Zymolyase 100T (Seikagaku Co., Tokyo, Japan) in PB for 30

671   min. Because the cell walls were not removed well, the cells were further treated with 1

672   mg/mL Zymolyase 100T in PB for 30 min at 30°C, with 0.2 mg/ml Lysing Enzyme for 30 min,

673   and washed with PB three times. After treatment with 100 mM lysine HCl in PB twice for 10

674   min and subsequent washing with PB, cells were permeabilized for 15 min with PB

675   containing 0.2% saponin and 1% bovine serum albumin (BSA), and incubated at 4°C

676   overnight with primary antibody (rabbit polyclonal anti-GFP antibody; Rockland) diluted

677   1:400 in PB containing 1% BSA and 0.01% saponin. After washing with PB containing

678   0.005% saponin three times for 10 min each, cells were incubated for 2 hours at room

679   temperature with secondary antibody (goat anti-rabbit Alexa 594 FluoroNanogold Fab'

680   fragment, Nanoprobes, Yaphank, NY, USA) diluted 1:400 in PB containing 1% BSA and

681   0.01% saponin, washed with PB containing 0.005% saponin three times for 10 min each,

682   and with PB once. Then, the cells were fixed again with 1% glutaraldehyde in PB for 1 hour,

683   washed with PB once and treated with 100 mM lysine HCl in PB twice for 10 min each. The

684   cells were stored at 4°C until further use.

685   Before use, the cells were incubated with 50 mM HEPES (pH5.8) three times for 3

686   min each, washed with distilled water (dH2O) once, and then incubated at 25°C for 3 min

687   with the Silver enhancement reagent (an equal-volume mixture of the following solutions A,

688   B and C: A. 0.2% silver acetate solution. B. 2.8% trisodium citrate-2H_2O, 3% citric acid-H_2O,

689   and 0.5% hydroquinone. C. 300 mM HEPES, pH 8.2). Cells were then washed with dH2O

690   three times. Cells were embedded in 2% low melting agarose dissolved in dH2O. Then, cells

691   were post-fixed with 2% OsO4 in dH2O for 15 min at room temperature, washed with dH2O

692   three times, stained with 1% uranyl acetate in DW for 1 hour, and washed with dH2O three

693   times.

694   Cells were dehydrated by sequential incubation in 50 and 100% ethanol for 10 min

695   each, and with acetone for 10 min. For embedding in epoxy resin, cells were incubated

696   sequentially with mixtures of acetone: Epon812 (1:1) for 1hr, acetone:Epon812 (1:2) for 1hr,

697   and Epon812 overnight, and then Epon812 again for another 3 hours, and left to stand until

698   solidified. The block containing cells was sectioned with a microtome (Leica Microsystems),

699   and the ultra-thin sections were doubly stained with 4% uranyl acetate for 20 min and lead

700   citrate (Sigma, Tokyo Japan) for 1 min as usually treated in EM methods. Images were

701   obtained using a JEM1400 transmission electron microscope (JEOL, Tokyo, Japan)

702   at 120kV.

703

Biochemistry and mass spectrometry

Cell harvesting and cryogrinding

706   Cell cultures in late exponential growth were collected by centrifugation at 5000 rpm

707   for 15 mins at 4°C in a JLA-8.1000 rotor (Beckman Coulter). Cell pellets were resuspended

708   in one-quarter culture volume of wash buffer (10mM $NaPO_4$ pH 7.5 and 0.5 mM EDTA) and

709   then washed three times by centrifugation at 5000 rpm for 15 mins at 4°C in a JLA-10.500

710   rotor (Beckman Coulter) and resuspension in the same volume of wash buffer. After the final

711   centrifugation, the cell pellet was weighed and resuspended in wash buffer, using a ratio of

712   0.3 mL wash buffer per gram of cell pellet. The cell suspension was then quick-frozen by

713   drop-wise addition into liquid nitrogen and stored at -80°C until further use.

714   Cryogrinding was performed using an RM100 electric mortar grinder with a zirconium

715   oxide mortar and pestle (Retsch). The mortar and pestle were pre-cooled by filling with liquid

716   nitrogen for 10 min before grinding. Frozen cells were then added into the pre-cooled grinder

717   and ground for 40 min, with regular generous addition of liquid nitrogen to maintain the

718   temperature and prevent cell clumping during the grinding process. Cryogrindate cell powder

719   was recovered and stored at -80°C until further use.

720

Anti-GFP immunoprecipitation (for preliminary SILAC interactome analysis)

722   Large-scale anti-GFP immunoprecipitation was performed using homemade sheep

723   anti-GFP antibody covalently coupled to Protein G Dynabeads (Thermo Fisher Scientific)

724   using dimethylpimelimidate (Borek et al., 2015). Immunoprecipitation (IP) buffer contained

725   15 mM $NaPO_4$ pH 7.5, 100 mM KCl, 0.5 mM EDTA, 0.2% TX-100, 10 µg/mL CLAAPE

726   protease inhibitors (chymostatin, leupeptin, antipain dihydrochloride, aprotinin, pepstatin, E-

727   64), 2 mM AEBSF, 2 mM PMSF, 1 mM NaF, 50 nM calyculin A, 50 nM okadaic acid, 0.1 mM

728   Na_3VO_4, and 2 mM benzamidine.

729   After SILAC labeling, cell harvesting and cryogrinding, 37 g of cell cryogrindate

730   powder was mixed with 66.6 ml of cold (4°C) IP buffer and vortexed until dissolved. Cell

731   lysate was then centrifuged at 13,000 rpm for 15 min at 4°C to remove most of the cell

732   debris. The supernatant was transferred to a fresh tube and centrifuged again at 13,000 rpm

733   for 15 min at 4°C, and the second supernatant was recovered. Protein concentration of

734   clarified lysates was measured by Bradford assay and then normalized by adding

735   appropriate volume of IP buffer as necessary.

736   For immunoprecipitation, 140 µL of anti-GFP/Protein G-Dynabead slurry (~2.1x10^9

737   beads, coupled to ~85 µg of antibody) were washed twice with 0.5 mL of IP buffer, mixed

738   with 70 mL of clarified cell lysate, and incubated at 4°C for 1.5 h with gentle rotation. Beads

739   were then collected with a magnet, washed three times with 1 mL IP buffer, transferred to a

740   fresh microfuge tube, and washed twice again with 1 mL IP buffer. The beads were then

741   centrifuged at 13,000 rpm for 10 s, and any remaining buffer was removed.

742   To elute proteins from beads, a total of 65 µL Laemmli sample buffer (LSB; 2% SDS

743   (v/v), 10% glycerol, 62.5 mM Tris pH 6.8) was added to beads, which were then mixed by

744   pipetting and incubated at 65°C for 15 min with intermittent vortexing. The mixture was then

745   briefly centrifuged before transferring the supernatant to a fresh microfuge tube, and DTT

746   and bromophenol blue were added to final concentrations of 0.1 M and 0.01%, respectively.

747   This final sample was then heated at 95°C for 5 min and stored at -20°C prior to SDS-PAGE.

748   Samples from large-scale immunoprecipitations were processed for SILAC mass

749   spectrometry analysis as described below.

750

751   ***Cryogrindate cross-linking in vitro***

752   A 0.125 M stock solution of disuccinimidyl suberate (DSS; Thermo Fisher Scientific)

753   was made fresh in DMSO. Just before cross-linking, this was diluted to 2.5 mM final

754   concentration in cross-linking buffer (15 mM NaPO4 pH 7.5, 85 mM NaCl, 0.2% Triton X-

755   100, 1 mM PMSF, 10 µg/mL CLAAPE protease inhibitors, 2 mM AEBSF, 1 mM NaF, 50 nM

756   okadaic acid, 0.1 mM Na_3VO_4 and 2 mM benzamidine). 6 g of cell cryogrindate powder was

757   resuspended in 6 mL of cross-linking buffer containing DSS and mixed by vortexing. Cell

758   lysate was then incubated at 4°C for 2 h with gentle rotation. Then, 1.2 mL of 1.5 M Tris-HCl

759   pH 8.8 was added to the cell lysate to quench the cross-linking reaction, and left at room

760   temperature for 30 min. The cross-linked cell lysate was then used for two-step purification

761   as described below.

762

763   ***Two-step purification of HTB-tagged Mto1 variants***

764   HTB-tagged Mto1 variants were purified in two steps, using nickel-charged Fractogel

765   EMD Chelate (M) (Merck) resin and Nanolink magnetic streptavidin beads (Solulink), under

766   denaturing conditions. The procedure described below was used for purifications after

767   cryogrindate cross-linking *in vitro*, which was most commonly used. For purifications after

768   cross-linking *in vivo*, the same approach was used, but all amounts and volumes were

769   doubled (this is because initial purifications were done after cross-linking *in vivo*, and it was

770   later determined that half as much material was still sufficient for MS analysis)

771   For the first-step purification, 12 mL of cross-linked and quenched cell lysate

772   (representing 6 g cryogrindate) was mixed with 60 mL guanidine purification buffer (6 M

773   guanidine, 15 mM $NaPO_4$ pH 7.5, 85 mM NaCl, 0.5% TritonX-100, 1 mM PMSF, 1 mM NaF,

774   0.1 mM Na_3VO_4 and 2 mM benzamidine). The cell lysate was then sonicated with a Sonics

775   VC505 sonicator fitted with a 3mm tip for 2 min (1 s on, 1 s off, for total time 4 min, at 60%

776   amplification), centrifuged at 4,000 rpm for 15 min at room temperature to remove cell

777   debris, and the supernatant was recovered. 1.2 mL of 50% slurry of Fractogel EMD Chelate

778   (henceforth referred to as "Fractogel") was charged with nickel and washed twice with 5 mL

779   distilled water, and twice with 5 mL guanidine purification buffer. The charged Fractogel bed

780   was resuspended with an equal volume of 6 M guanidine purification buffer and mixed with

781   the lysate supernatant and incubated at room temperature for 2 h, with gentle rotation. The

782   suspension was then transferred to a 20 mL disposable plastic column (Evergreen

783   Scientific), washed once with 20 mL of 6 M guanidine purification buffer, and washed 3 times

784   with 20 mL of 8M urea purification buffer (contained 8 M urea, 15 mM $NaPO_4$ pH 7.5, 85 mM

785   NaCl, 0.1% TritonX-100, 1 mM PMSF, 1 mM NaF, 0.1 mM Na_3VO_4 and 2 mM benzamidine).

786   The Fractogel was then resuspended in 1 mL of 8 M urea purification buffer and transferred

787   into a 15 mL polypropylene tube. This process was repeated for 2 more times to recover all

788   of the Fractogel from the column. Fractogel was then centrifuged at 4,000 rpm for 3 min at

789   RT. The supernatant was discarded, and 3 mL of LSB containing 600 mM imidazole was

790   added to the tube, and bound proteins were eluted by heating at 95°C for 5 min. The

791   Fractogel was then centrifuged at 4,000 rpm for 3 min, and the supernatant was recovered,

792   quick-frozen in liquid nitrogen, and stored at -80°C.

793   For the second-step purification, the stored elution from the first-step purification

794   above was thawed at room temperature, and TX-100 was added to a final concentration of

795   1%. 30 µL of Nanolink streptavidin beads slurry (as supplied by manufacturer; this

796   corresponds to ~1.2 µL bed volume) was washed twice with 1 mL of LSB containing 1% TX-

797   100, resuspended into 30 µL of LSB containing 1% TX-100 and added to the thawed first-

798   step elution. This suspension was incubated for 1.5 h at room temperature, then collected

799   with a magnet and washed once with 1 mL of LSB and three times with 1 mL of LSB without

800   glycerol. After transfer to a microfuge tube, beads were resuspended in 15 µL of LSB and

801   heated at 95°C for 5 min. The elution from the beads was collected and DTT and

802   bromophenol blue were added, to final concentrations of 0.1M and 0.01%, respectively. The

803   mixture was boiled again for 5 min and stored at -20°C prior to SDS-PAGE.

804

805   ***Mass spectrometry (label-free quantification)***

806   For label-free quantification mass spectrometry analysis of samples after two-step

807   purification, ~18 µL of second-step elution was loaded onto a single lane (~0.5 cm wide) of a

808   4-20% Tris-glycine polyacrylamide gel (Biorad). Samples were run at 150V for 12-14 min.

809   The gel was stained with Coomassie Blue at room temperature for 1 h and destained in 10%

810   acetic acid overnight. On the following day, the gel was washed once in distilled water and

811   the relevant region recovered after excision with a clean scalpel. In general, for all samples,

812   we recovered the region of the gel above, but not including, the non-cross-linked Mto1 band,

813   in order to increase the relative proportion of cross-linked Mto1 species vs. non-crosslinked

814   Mto1.

815   Excised gel bands were destained with 50mM ammonium bicarbonate (Sigma

816   Aldrich, UK) and 100% (v/v) acetonitrile (Sigma Aldrich, UK) and proteins were digested with

817   trypsin, as previously described (Shevchenko et al., 1996). In brief, proteins were reduced in

818   10 mM dithiothreitol (Sigma Aldrich, UK) for 30 min at 37°C and alkylated in 55 mM

819   iodoacetamide (Sigma Aldrich, UK) for 20 min at ambient temperature in the dark. They

820   were then digested overnight at 37°C with 13 ng/μL trypsin (Pierce, UK).

821   Following digestion, samples were diluted with an equal volume of 0.1% TFA and

822   spun onto StageTips as described (Rappsilber et al., 2003). Peptides were eluted in 40 μL of

823   80% acetonitrile in 0.1% TFA and concentrated to 1 μL by vacuum centrifugation

824   (Concentrator 5301, Eppendorf, UK). Samples were then prepared for LC-MS/MS analysis

825   by diluting to 5 μL with 0.1% TFA. LC-MS-analyses were performed on a Q Exactive mass

826   spectrometer (Thermo Fisher Scientific, UK) (Figures 1, 3, and 6) and on an Orbitrap

827   Fusion™ Lumos™ Tribrid™ Mass Spectrometer (Thermo Fisher Scientific, UK) (Figure 4),

828   both coupled on-line to Ultimate 3000 RSLCnano Systems (Dionex, Thermo Fisher

829   Scientific, UK). Peptides were separated on a 50 cm EASY-Spray column (Thermo

830   Scientific, UK) assembled in an EASY-Spray source (Thermo Scientific, UK) and operated at

831   50^oC. In both cases, mobile phase A consisted of 0.1% formic acid in water while mobile

832   phase B consisted of 80% acetonitrile and 0.1% formic acid. Peptides were loaded onto the

833   column at a flow rate of 0.3 μL/min and eluted at a flow rate of 0.2 μL/min according to the

834   following gradients: 2 to 40% buffer B in 90 min, then to 95% buffer B in 11 min (Figures 1, 3

835   and 4) and 2 to 40% buffer B in 120 min and then to 95% buffer B in 11 min (Figure 6). For

836   Q Exactive, FTMS spectra were recorded at 70,000 resolution (scan range 350-1400 m/z)

837   and the ten most intense peaks with charge ≥ 2 of the MS scan were selected with an

838   isolation window of 2.0 Thomson for MS2 (filling 1.0E6 ions for MS scan, 5.0E4 ions for

839   MS2, maximum fill time 60 ms, dynamic exclusion for 50 s). For Orbitrap Fusion Lumos,

840   survey scans were performed at 60,000 resolution (scan range 350-1400 m/z) with an ion

841   target of 7.0e5. MS2 was performed in the orbitrap with ion target of 5.0E3 and HCD

842   fragmentation with normalized collision energy of 25 (Olsen et al., 2007). The isolation

843   window in the quadrupole was 1.6. Only ions with charge between 2 and 7 were selected for

844   MS2.

845   The MaxQuant software platform (Cox & Mann, 2008) version 1.5.2.8 was used to

846   process raw files, and search was conducted against *Schizosaccharomyces pombe*

847   complete/reference proteome set from PomBase (www.pombase.org; released in July,

848   2016), using the Andromeda search engine (Cox et al., 2011). The first search peptide

849   tolerance was set to 20 ppm while the main search peptide tolerance was set to 4.5 ppm.

850   Isotope mass tolerance was set to 2 ppm, and maximum charge state was set to 7.

851   Maximum of two missed cleavages were allowed. Carbamidomethylation of cysteine was set

852   as fixed modification. Oxidation of methionine and acetylation of the N-terminal were set as

853   variable modifications. Label-free quantification analysis was performed by employing the

854   MaxLFQ algorithm as described (Cox et al., 2014). Peptide and protein identifications were

855   filtered to 1% FDR.

856   All LFQ MS was performed using two complete biological replicates of each of the

857   two conditions being compared. For experiments shown in Fig. 6, additional biological

858   replicates using cells grown in LowN medium were also performed, alongside those using

859   cells grown in PMG (as normal). Including the LowN replicates during MaxQuant analysis

860   improved the quality of peptide identifications from experiments using cells grown in PMG.

861   Data shown in Fig. 6 are only from cells grown in PMG; however, data from cells grown in

862   LowN are completely consistent with the data from cells grown in PMG and are included with

863   the PMG data as part of Supplementary File 6.

864   Scatterplots showing LFQ ratio vs. LFQ intensity (Figs. 1, 3, 4, 6) were constructed

865   as follows: In cases where the relevant Mto1-interactors (e.g. Crm1, Nup146) were fully

866   quantified in both conditions of both replicate experiments (i.e. Figs. 3 & 6), the values

867   shown in scatterplots represent the geometric mean from the two replicates. The geometric

868   mean was used rather than the arithmetic mean in order to minimize any effects of extreme

869   outliers. In other cases (i.e. Figs. 1 & 4), Nup146 was not fully quantified in one of the

870   conditions of one of the replicate experiments, because of low signal intensity or low peptide

871   count. In these cases, it was not possible to calculate mean LFQ values for Nup146 from

872   replicate experiments, and therefore, the values shown in scatterplots are taken from the

873   replicate in which the Nup146 was fully quantified. Summary tables showing peptide counts

874   and LFQ values from all replicate experiments are shown in Supplementary Figures, and full

875   datasets, including LFQ values, are provided in Supplementary Files.

876

877   ***Mass spectrometry (SILAC)***

878   To generate the SILAC data shown in Supplementary File 2 (preliminary results, from

879   anti-GFP immunoprecipitation), sample processing and digestion was performed as

880   described above. LC-MS analyses were performed on a Q Exactive mass spectrometer

881   (Thermo Fisher Scientific, UK) coupled on-line, to Ultimate 3000 RSLCnano Systems

882   (Dionex, Thermo Fisher Scientific, UK). The analytical column with a self-assembled particle

883   frit (Ishihama et al., 2002) and C18 material (ReproSil-Pur C18-AQ 3 µm; Dr. Maisch,

884   GmbH, Germany) was packed into a spray emitter (75-µm ID, 8-µm opening, 300-mm

885   length; New Objective) using an air-pressure pump (Proxeon Biosystems, USA). Mobile

886   phase A consisted of 0.1% formic acid in water while mobile phase B consisted of 80%

887 acetonitrile and 0.1% formic acid. Peptides were loaded onto the column at a flow rate of 0.5

888 μL/min and eluted at a flow rate of 0.2 μL/min according to the following gradient: 2 to 40% in

889 120 min and then to 95% in 11 min. The settings on the Q Exactive were the same as

890 described above.

891 The MaxQuant software platform (Cox & Mann, 2008) version 1.3.0.5 was used to

892 process raw files, and search was conducted against *Schizosaccharomyces pombe*

893 complete/reference proteome set from PomBase (released in August, 2012), using the

894 Andromeda search engine (Cox et al., 2011). The first search peptide tolerance was set to

895 20 ppm, while the main search peptide tolerance was set to 4.5 ppm. Isotope mass

896 tolerance was 2 ppm and maximum charge was set to 7. The MS/MS match tolerance was

897 set to 20 ppm, and two missed cleavages were allowed. Carbamidomethylation of cysteine

898 was set as fixed modification, and oxidation of methionine with acetylation of the N-terminal

899 were set as variable modifications. Multiplicity was set to 2, and for heavy labels, Arginine-6

900 and Lysine-8 were selected, and peptide and protein identifications were filtered to 1% FDR.

901 Unique and non-unique peptides were used for quantification. Proteins with minimum of two

902 quantified labeled peptide pairs/triplets were reported for quantification, and the isoforms

903 with the highest peptide counts were considered for quantification.

904

905 **ACKNOWLEDGEMENTS**

914

915 **REFERENCES**

916 Adachi Y, Yanagida M (1989) Higher order chromosome structure is affected by cold-
917   sensitive mutations in a Schizosaccharomyces pombe gene crm1+ which encodes a 115-
918   kD protein preferentially localized in the nucleus and its periphery. J Cell Biol 108: 1195-
919   207
920 Adams RL, Terry LJ, Wente SR (2014) Nucleoporin FG domains facilitate mRNP remodeling
921   at the cytoplasmic face of the nuclear pore complex. Genetics 197: 1213-24
922 Aitchison JD, Rout MP (2012) The yeast nuclear pore complex and transport through it.
923   Genetics 190: 855-83
924 Allen NP, Patel SS, Huang L, Chalkley RJ, Burlingame A, Lutzmann M, Hurt EC, Rexach M
925   (2002) Deciphering networks of protein interactions at the nuclear pore complex. Mol Cell
926   Proteomics 1: 930-46

927 Ambrose C, Wasteneys GO (2014) Microtubule initiation from the nuclear surface controls
928   cortical microtubule growth polarity and orientation in Arabidopsis thaliana. Plant Cell
929   Physiol 55: 1636-45
930 Arnaoutov A, Azuma Y, Ribbeck K, Joseph J, Boyarchuk Y, Karpova T, McNally J, Dasso M
931   (2005) Crm1 is a mitotic effector of Ran-GTP in somatic cells. Nat Cell Biol 7: 626-32
932 Asakawa H, Yang HJ, Yamamoto TG, Ohtsuki C, Chikashige Y, Sakata-Sogawa K,
933   Tokunaga M, Iwamoto M, Hiraoka Y, Haraguchi T (2014) Characterization of nuclear pore
934   complex components in fission yeast Schizosaccharomyces pombe. Nucleus 5: 149-62
935 Askjaer P, Bachi A, Wilm M, Bischoff FR, Weeks DL, Ogniewski V, Ohno M, Niehrs C,
936   Kjems J, Mattaj IW, Fornerod M (1999) RanGTP-regulated interactions of CRM1 with
937   nucleoporins and a shuttling DEAD-box helicase. Mol Cell Biol 19: 6276-85
938 Bahler J, Wu JQ, Longtine MS, Shah NG, McKenzie A, 3rd, Steever AB, Wach A, Philippsen
939   P, Pringle JR (1998) Heterologous modules for efficient and versatile PCR-based gene
940   targeting in Schizosaccharomyces pombe. Yeast 14: 943-51
941 Bai SW, Rouquette J, Umeda M, Faigle W, Loew D, Sazer S, Doye V (2004) The fission
942   yeast Nup107-120 complex functionally interacts with the small GTPase Ran/Spi1 and is
943   required for mRNA export, nuclear pore distribution, and proper cell division. Mol Cell Biol
944   24: 6379-92
945 Bartolini F, Gundersen GG (2006) Generation of noncentrosomal microtubule arrays. J Cell
946   Sci 119: 4155-63
947 Bernad R, Engelsma D, Sanderson H, Pickersgill H, Fornerod M (2006) Nup214-Nup88
948   nucleoporin subcomplex is required for CRM1-mediated 60 S preribosomal nuclear
949   export. J Biol Chem 281: 19378-86
950 Bicho CC, de Lima Alves F, Chen ZA, Rappsilber J, Sawin KE (2010) A genetic engineering
951   solution to the "arginine conversion problem" in stable isotope labeling by amino acids in
952   cell culture (SILAC). Mol Cell Proteomics 9: 1567-77
953 Bischoff FR, Klebe C, Kretschmer J, Wittinghofer A, Ponstingl H (1994) RanGAP1 induces
954   GTPase activity of nuclear Ras-related Ran. Proc Natl Acad Sci U S A 91: 2587-91
955 Borek WE, Groocock LM, Samejima I, Zou J, de Lima Alves F, Rappsilber J, Sawin KE
956   (2015) Mto2 multisite phosphorylation inactivates non-spindle microtubule nucleation
957   complexes during mitosis. Nat Commun 6: 7929
958 Bugnard E, Zaal KJ, Ralston E (2005) Reorganization of microtubule nucleation during
959   muscle differentiation. Cell Motil Cytoskeleton 60: 1-13
960 Cavazza T, Vernos I (2015) The RanGTP Pathway: From Nucleo-Cytoplasmic Transport to
961   Spindle Assembly and Beyond. Front Cell Dev Biol 3: 82
962 Chang F, Martin SG (2009) Shaping fission yeast with microtubules. Cold Spring Harb
963   Perspect Biol 1: a001347
964 Chen XQ, Du X, Liu J, Balasubramanian MK, Balasundaram D (2004) Identification of genes
965   encoding putative nucleoporins and transport factors in the fission yeast
966   Schizosaccharomyces pombe: a deletion analysis. Yeast 21: 495-509
967 Choi YK, Liu P, Sze SK, Dai C, Qi RZ (2010) CDK5RAP2 stimulates microtubule nucleation
968   by the gamma-tubulin ring complex. J Cell Biol 191: 1089-95
969 Clarke PR, Klebe C, Wittinghofer A, Karsenti E (1995) Regulation of Cdc2/cyclin B activation
970   by Ran, a Ras-related GTPase. J Cell Sci 108 (Pt 3): 1217-25
971 Cox J, Hein MY, Luber CA, Paron I, Nagaraj N, Mann M (2014) Accurate proteome-wide
972   label-free quantification by delayed normalization and maximal peptide ratio extraction,
973   termed MaxLFQ. Mol Cell Proteomics 13: 2513-26
974 Cox J, Mann M (2008) MaxQuant enables high peptide identification rates, individualized
975   p.p.b.-range mass accuracies and proteome-wide protein quantification. Nat Biotechnol
976   26: 1367-72
977 Cox J, Neuhauser N, Michalski A, Scheltema RA, Olsen JV, Mann M (2011) Andromeda: a
978   peptide search engine integrated into the MaxQuant environment. J Proteome Res 10:
979   1794-805
980 Daga RR, Chang F (2005) Dynamic positioning of the fission yeast cell division plane. Proc
981   Natl Acad Sci U S A 102: 8228-32

982   Dasso M, Seki T, Azuma Y, Ohba T, Nishimoto T (1994) A mutant form of the Ran/TC4
983   protein disrupts nuclear function in Xenopus laevis egg extracts by inhibiting the RCC1
984   protein, a regulator of chromosome condensation. Embo J 13: 5732-44
985   Dong X, Biswas A, Suel KE, Jackson LK, Martinez R, Gu H, Chook YM (2009) Structural
986   basis for leucine-rich nuclear export signal recognition by CRM1. Nature 458: 1136-41
987   Ekwall K, Thon G (2017) Genetic Analysis of Schizosaccharomyces pombe. Cold Spring
988   Harb Protoc 2017: pdb top079772
989   Engelsma D, Bernad R, Calafat J, Fornerod M (2004) Supraphysiological nuclear export
990   signals bind CRM1 independently of RanGTP and arrest at Nup358. Embo J 23: 3643-52
991   Engelsma D, Valle N, Fish A, Salome N, Almendral JM, Fornerod M (2008) A
992   supraphysiological nuclear export signal is required for parvovirus nuclear export. Mol
993   Biol Cell 19: 2544-52
994   Erhardt M, Stoppin-Mellet V, Campagne S, Canaday J, Mutterer J, Fabian T, Sauter M,
995   Muller T, Peter C, Lambert AM, Schmit AC (2002) The plant Spc98p homologue
996   colocalizes with gamma-tubulin at microtubule nucleation sites and is required for
997   microtubule nucleation. J Cell Sci 115: 2423-31
998   Fant X, Srsen V, Espigat-Georger A, Merdes A (2009) Nuclei of non-muscle cells bind
999   centrosome proteins upon fusion with differentiating myoblasts. PLoS One 4: e8303
1000   Fennessy D, Grallert A, Krapp A, Cokoja A, Bridge AJ, Petersen J, Patel A, Tallada VA,
1001   Boke E, Hodgson B, Simanis V, Hagan IM (2014) Extending the Schizosaccharomyces
1002   pombe molecular genetic toolbox. PLoS One 9: e97683
1003   Forbes DJ, Travesa A, Nord MS, Bernis C (2015) Nuclear transport factors: global regulation
1004   of mitosis. Curr Opin Cell Biol 35: 78-90
1005   Fornerod M, Ohno M, Yoshida M, Mattaj IW (1997a) CRM1 is an export receptor for leucine-
1006   rich nuclear export signals. Cell 90: 1051-60
1007   Fornerod M, van Deursen J, van Baal S, Reynolds A, Davis D, Murti KG, Fransen J,
1008   Grosveld G (1997b) The human homologue of yeast CRM1 is in a dynamic subcomplex
1009   with CAN/Nup214 and a novel nuclear pore component Nup88. Embo J 16: 807-16
1010   Forsburg SL, Rhind N (2006) Basic methods for fission yeast. Yeast 23: 173-83
1011   Fukuda M, Asano S, Nakamura T, Adachi M, Yoshida M, Yanagida M, Nishida E (1997)
1012   CRM1 is responsible for intracellular transport mediated by the nuclear export signal.
1013   Nature 390: 308-11
1014   Fung HY, Chook YM (2014) Atomic basis of CRM1-cargo recognition, release and inhibition.
1015   Semin Cancer Biol 27: 52-61
1016   Fung HY, Fu SC, Brautigam CA, Chook YM (2015) Structural determinants of nuclear export
1017   signal orientation in binding to exportin CRM1. Elife 4
1018   Fung HY, Fu SC, Chook YM (2017) Nuclear export receptor CRM1 recognizes diverse
1019   conformations in nuclear export signals. Elife 6
1020   Gorlich D, Kutay U (1999) Transport between the cell nucleus and the cytoplasm. Annu Rev
1021   Cell Dev Biol 15: 607-60
1022   Gorsch LC, Dockendorff TC, Cole CN (1995) A conditional allele of the novel repeat-
1023   containing yeast nucleoporin RAT7/NUP159 causes both rapid cessation of mRNA export
1024   and reversible clustering of nuclear pore complexes. J Cell Biol 129: 939-55
1025   Goshima G, Mayer M, Zhang N, Stuurman N, Vale RD (2008) Augmin: a protein complex
1026   required for centrosome-independent microtubule generation within the spindle. J Cell
1027   Biol 181: 421-9
1028   Guttler T, Gorlich D (2011) Ran-dependent nuclear export mediators: a structural
1029   perspective. Embo J 30: 3457-74
1030   Guttler T, Madl T, Neumann P, Deichsel D, Corsini L, Monecke T, Ficner R, Sattler M,
1031   Gorlich D (2010) NES consensus redefined by structures of PKI-type and Rev-type
1032   nuclear export signals bound to CRM1. Nat Struct Mol Biol 17: 1367-76
1033   Hopper AK, Traglia HM, Dunst RW (1990) The yeast RNA1 gene product necessary for
1034   RNA processing is located in the cytosol and apparently excluded from the nucleus. J
1035   Cell Biol 111: 309-21

1036 Hutten S, Kehlenbach RH (2006) Nup214 is required for CRM1-dependent nuclear protein
1037   export in vivo. Mol Cell Biol 26: 6772-85
1038 Hutten S, Kehlenbach RH (2007) CRM1-mediated nuclear export: to the pore and beyond.
1039   Trends Cell Biol 17: 193-201
1040 Ishihama Y, Rappsilber J, Andersen JS, Mann M (2002) Microcolumns with self-assembled
1041   particle frits for proteomics. J Chromatogr A 979: 233-9
1042 Janski N, Masoud K, Batzenschlager M, Herzog E, Evrard JL, Houlne G, Bourge M,
1043   Chaboute ME, Schmit AC (2012) The GCP3-interacting proteins GIP1 and GIP2 are
1044   required for gamma-tubulin complex protein localization, spindle integrity, and
1045   chromosomal stability. Plant Cell 24: 1171-87
1046 Janson ME, Setty TG, Paoletti A, Tran PT (2005) Efficient formation of bipolar microtubule
1047   bundles requires microtubule-bound gamma-tubulin complexes. J Cell Biol 169: 297-308
1048 Kalab P, Heald R (2008) The RanGTP gradient - a GPS for the mitotic spindle. J Cell Sci
1049   121: 1577-86
1050 Kapitein LC, Hoogenraad CC (2015) Building the Neuronal Microtubule Cytoskeleton.
1051   Neuron 87: 492-506
1052 Kehlenbach RH, Dickmanns A, Kehlenbach A, Guan T, Gerace L (1999) A role for RanBP1
1053   in the release of CRM1 from the nuclear pore complex in a terminal step of nuclear
1054   export. J Cell Biol 145: 645-57
1055 Klebe C, Bischoff FR, Ponstingl H, Wittinghofer A (1995) Interaction of the nuclear GTP-
1056   binding protein Ran with its regulatory proteins RCC1 and RanGAP1. Biochemistry 34:
1057   639-47
1058 Knauer SK, Bier C, Habtemichael N, Stauber RH (2006) The Survivin-Crm1 interaction is
1059   essential for chromosomal passenger complex localization and function. EMBO Rep 7:
1060   1259-65
1061 Kollman JM, Merdes A, Mourey L, Agard DA (2011) Microtubule nucleation by gamma-
1062   tubulin complexes. Nat Rev Mol Cell Biol 12: 709-21
1063 Kornbluth S, Dasso M, Newport J (1994) Evidence for a dual role for TC4 protein in
1064   regulating nuclear structure and cell cycle progression. J Cell Biol 125: 705-19
1065 Koyama M, Matsuura Y (2012) Mechanistic insights from the recent structures of the CRM1
1066   nuclear export complex and its disassembly intermediate. Biophysics (Nagoya-shi) 8:
1067   145-50
1068 Kraemer D, Wozniak RW, Blobel G, Radu A (1994) The human CAN protein, a putative
1069   oncogene product associated with myeloid leukemogenesis, is a nuclear pore complex
1070   protein that faces the cytoplasm. Proc Natl Acad Sci U S A 91: 1519-23
1071 Kraemer DM, Strambio-de-Castillia C, Blobel G, Rout MP (1995) The essential yeast
1072   nucleoporin NUP159 is located on the cytoplasmic side of the nuclear pore complex and
1073   serves in karyopherin-mediated binding of transport substrate. J Biol Chem 270: 19017-
1074   21
1075 Kudo N, Matsumori N, Taoka H, Fujiwara D, Schreiner EP, Wolff B, Yoshida M, Horinouchi
1076   S (1999) Leptomycin B inactivates CRM1/exportin 1 by covalent modification at a
1077   cysteine residue in the central conserved region. Proc Natl Acad Sci U S A 96: 9112-7
1078 Kutay U, Guttinger S (2005) Leucine-rich nuclear-export signals: born to be weak. Trends
1079   Cell Biol 15: 121-4
1080 Lin TC, Neuner A, Schiebel E (2015) Targeting of gamma-tubulin complexes to microtubule
1081   organizing centers: conservation and divergence. Trends Cell Biol 25: 296-307
1082 Ling YC, Vjestica A, Oliferenko S (2009) Nucleocytoplasmic shuttling of the TACC protein
1083   Mia1p/Alp7p is required for remodeling of microtubule arrays during the cell cycle. PLoS
1084   One 4: e6255
1085 Liu T, Tian J, Wang G, Yu Y, Wang C, Ma Y, Zhang X, Xia G, Liu B, Kong Z (2014) Augmin
1086   triggers microtubule-dependent microtubule nucleation in interphase plant cells. Curr Biol
1087   24: 2708-13
1088 Lo Presti L, Chang F, Martin SG (2012) Myosin Vs organize actin cables in fission yeast. Mol
1089   Biol Cell 23: 4579-91

1090 Lynch EM, Groocock LM, Borek WE, Sawin KE (2014) Activation of the gamma-tubulin
1091   complex by the Mto1/2 complex. Curr Biol 24: 896-903
1092 Masoud K, Herzog E, Chaboute ME, Schmit AC (2013) Microtubule nucleation and
1093   establishment of the mitotic spindle in vascular plant cells. Plant J 75: 245-57
1094 Matsumoto T, Beach D (1991) Premature initiation of mitosis in yeast lacking RCC1 or an
1095   interacting GTPase. Cell 66: 347-60
1096 Matsuyama A, Arai R, Yashiroda Y, Shirai A, Kamata A, Sekido S, Kobayashi Y, Hashimoto
1097   A, Hamamoto M, Hiraoka Y, Horinouchi S, Yoshida M (2006) ORFeome cloning and
1098   global analysis of protein localization in the fission yeast Schizosaccharomyces pombe.
1099   Nat Biotechnol 24: 841-7
1100 Mogessie B, Roth D, Rahil Z, Straube A (2015) A novel isoform of MAP4 organises the
1101   paraxial microtubule array required for muscle cell differentiation. Elife 4: e05697
1102 Monecke T, Dickmanns A, Ficner R (2014) Allosteric control of the exportin CRM1 unraveled
1103   by crystal structure analysis. FEBS J 281: 4179-94
1104 Monecke T, Guttler T, Neumann P, Dickmanns A, Gorlich D, Ficner R (2009) Crystal
1105   structure of the nuclear export receptor CRM1 in complex with Snurportin1 and RanGTP.
1106   Science 324: 1087-91
1107 Monecke T, Haselbach D, Voss B, Russek A, Neumann P, Thomson E, Hurt E, Zachariae U,
1108   Stark H, Grubmuller H, Dickmanns A, Ficner R (2013) Structural basis for cooperativity of
1109   CRM1 export complex formation. Proc Natl Acad Sci U S A 110: 960-5
1110 Nakamura M, Yagi N, Kato T, Fujita S, Kawashima N, Ehrhardt DW, Hashimoto T (2012)
1111   Arabidopsis GCP3-interacting protein 1/MOZART 1 is an integral component of the
1112   gamma-tubulin-containing microtubule nucleating complex. Plant J 71: 216-25
1113 Napetschnig J, Blobel G, Hoelz A (2007) Crystal structure of the N-terminal domain of the
1114   human protooncogene Nup214/CAN. Proc Natl Acad Sci U S A 104: 1783-8
1115 Oda Y (2015) Cortical microtubule rearrangements and cell wall patterning. Front Plant Sci
1116   6: 236
1117 Ohkura H, Hagan IM, Glover DM (1995) The conserved Schizosaccharomyces pombe
1118   kinase plo1, required to form a bipolar spindle, the actin ring, and septum, can drive
1119   septum formation in G1 and G2 cells. Genes Dev 9: 1059-73
1120 Okada N, Sato M (2015) Spatiotemporal Regulation of Nuclear Transport Machinery and
1121   Microtubule Organization. Cells 4: 406-26
1122 Okada N, Toda T, Yamamoto M, Sato M (2014) CDK-dependent phosphorylation of Alp7-
1123   Alp14 (TACC-TOG) promotes its nuclear accumulation and spindle microtubule
1124   assembly. Mol Biol Cell 25: 1969-82
1125 Olsen JV, Macek B, Lange O, Makarov A, Horning S, Mann M (2007) Higher-energy C-trap
1126   dissociation for peptide modification analysis. Nat Methods 4: 709-12
1127 Ong SE, Blagoev B, Kratchmarova I, Kristensen DB, Steen H, Pandey A, Mann M (2002)
1128   Stable isotope labeling by amino acids in cell culture, SILAC, as a simple and accurate
1129   approach to expression proteomics. Mol Cell Proteomics 1: 376-86
1130 Ossareh-Nazari B, Bachelerie F, Dargemont C (1997) Evidence for a role of CRM1 in signal-
1131   mediated nuclear protein export. Science 278: 141-4
1132 Petersen J, Russell P (2016) Growth and the Environment of Schizosaccharomyces pombe.
1133   Cold Spring Harb Protoc 2016: pdb top079764
1134 Petry S, Vale RD (2015) Microtubule nucleation at the centrosome and beyond. Nat Cell Biol
1135   17: 1089-93
1136 Port SA, Monecke T, Dickmanns A, Spillner C, Hofele R, Urlaub H, Ficner R, Kehlenbach
1137   RH (2015) Structural and Functional Characterization of CRM1-Nup214 Interactions
1138   Reveals Multiple FG-Binding Sites Involved in Nuclear Export. Cell Rep 13: 690-702
1139 Rappsilber J, Ishihama Y, Mann M (2003) Stop and go extraction tips for matrix-assisted
1140   laser desorption/ionization, nanoelectrospray, and LC/MS sample pretreatment in
1141   proteomics. Anal Chem 75: 663-70
1142 Ren M, Coutavas E, D'Eustachio P, Rush MG (1994) Effects of mutant Ran/TC4 proteins on
1143   cell cycle progression. Mol Cell Biol 14: 4216-24

1144 Rivero S, Cardenas J, Bornens M, Rios RM (2009) Microtubule nucleation at the cis-side of
1145   the Golgi apparatus requires AKAP450 and GM130. Embo J 28: 1016-28
1146 Roloff S, Spillner C, Kehlenbach RH (2013) Several phenylalanine-glycine motives in the
1147   nucleoporin Nup214 are essential for binding of the nuclear export receptor CRM1. J Biol
1148   Chem 288: 3952-63
1149 Saito N, Matsuura Y (2013) A 2.1-A-resolution crystal structure of unliganded CRM1 reveals
1150   the mechanism of autoinhibition. J Mol Biol 425: 350-64
1151 Samejima I, Lourenco PC, Snaith HA, Sawin KE (2005) Fission yeast mto2p regulates
1152   microtubule nucleation by the centrosomin-related protein mto1p. Mol Biol Cell 16: 3040-
1153   51
1154 Samejima I, Miller VJ, Groocock LM, Sawin KE (2008) Two distinct regions of Mto1 are
1155   required for normal microtubule nucleation and efficient association with the gamma-
1156   tubulin complex in vivo. J Cell Sci 121: 3971-80
1157 Samejima I, Miller VJ, Rincon SA, Sawin KE (2010) Fission yeast Mto1 regulates diversity of
1158   cytoplasmic microtubule organizing centers. Curr Biol 20: 1959-65
1159 Sanchez AD, Feldman JL (2017) Microtubule-organizing centers: from the centrosome to
1160   non-centrosomal sites. Curr Opin Cell Biol 44: 93-101
1161 Sanchez-Huertas C, Freixo F, Viais R, Lacasa C, Soriano E, Luders J (2016) Non-
1162   centrosomal nucleation mediated by augmin organizes microtubules in post-mitotic
1163   neurons and controls axonal microtubule polarity. Nat Commun 7: 12187
1164 Sato M, Okada N, Kakui Y, Yamamoto M, Yoshida M, Toda T (2009) Nucleocytoplasmic
1165   transport of Alp7/TACC organizes spatiotemporal microtubule formation in fission yeast.
1166   EMBO Rep 10: 1161-7
1167 Sato M, Vardy L, Angel Garcia M, Koonrugsa N, Toda T (2004) Interdependency of fission
1168   yeast Alp14/TOG and coiled coil protein Alp7 in microtubule localization and bipolar
1169   spindle formation. Mol Biol Cell 15: 1609-22
1170 Sawin KE, Lourenco PC, Snaith HA (2004) Microtubule nucleation at non-spindle pole body
1171   microtubule-organizing centers requires fission yeast centrosomin-related protein
1172   mod20p. Curr Biol 14: 763-75
1173 Sawin KE, Nurse P (1998) Regulation of cell polarity by microtubules in fission yeast. J Cell
1174   Biol 142: 457-71
1175 Sawin KE, Tran PT (2006) Cytoplasmic microtubule organization in fission yeast. Yeast 23:
1176   1001-1014
1177 Schmitt C, von Kobbe C, Bachi A, Pante N, Rodrigues JP, Boscheron C, Rigaut G, Wilm M,
1178   Seraphin B, Carmo-Fonseca M, Izaurralde E (1999) Dbp5, a DEAD-box protein required
1179   for mRNA export, is recruited to the cytoplasmic fibrils of nuclear pore complex via a
1180   conserved interaction with CAN/Nup159p. Embo J 18: 4332-47
1181 Seltzer V, Janski N, Canaday J, Herzog E, Erhardt M, Evrard JL, Schmit AC (2007)
1182   Arabidopsis GCP2 and GCP3 are part of a soluble gamma-tubulin complex and have
1183   nuclear envelope targeting domains. Plant J 52: 322-31
1184 Shevchenko A, Wilm M, Vorm O, Mann M (1996) Mass spectrometric sequencing of proteins
1185   silver-stained polyacrylamide gels. Anal Chem 68: 850-8
1186 Srsen V, Fant X, Heald R, Rabouille C, Merdes A (2009) Centrosome proteins form an
1187   insoluble perinuclear matrix during muscle cell differentiation. BMC Cell Biol 10: 28
1188 Stade K, Ford CS, Guthrie C, Weis K (1997) Exportin 1 (Crm1p) is an essential nuclear
1189   export factor. Cell 90: 1041-50
1190 Stoppin V, Vantard M, Schmit AC, Lambert AM (1994) Isolated Plant Nuclei Nucleate
1191   Microtubule Assembly: The Nuclear Surface in Higher Plants Has Centrosome-like
1192   Activity. Plant Cell 6: 1099-1106
1193 Strawn LA, Shen T, Shulga N, Goldfarb DS, Wente SR (2004) Minimal nuclear pore
1194   complexes define FG repeat domains essential for transport. Nat Cell Biol 6: 197-206
1195 Tagwerker C, Flick K, Cui M, Guerrero C, Dou Y, Auer B, Baldi P, Huang L, Kaiser P (2006)
1196   A tandem affinity tag for two-step purification under fully denaturing conditions:
1197   application in ubiquitin profiling and protein complex identification combined with in
1198   vivocross-linking. Mol Cell Proteomics 5: 737-48

1199 Tange Y, Chikashige Y, Takahata S, Kawakami K, Higashi M, Mori C, Kojidani T, Hirano Y,
1200   Asakawa H, Murakami Y, Haraguchi T, Hiraoka Y (2016) Inner nuclear membrane protein
1201   Lem2 augments heterochromatin formation in response to nutritional conditions. Genes
1202   Cells 21: 812-32
1203 Tassin AM, Maro B, Bornens M (1985) Fate of microtubule-organizing centers during
1204   myogenesis in vitro. J Cell Biol 100: 35-46
1205 Tran PT, Marsh L, Doye V, Inoue S, Chang F (2001) A mechanism for nuclear positioning in
1206   fission yeast based on microtubule pushing. J Cell Biol 153: 397-411
1207 Tyanova S, Temu T, Cox J (2016) The MaxQuant computational platform for mass
1208   spectrometry-based shotgun proteomics. Nat Protoc 11: 2301-2319
1209 Venkatram S, Jennings JL, Link A, Gould KL (2005) Mto2p, a novel fission yeast protein
1210   required for cytoplasmic microtubule organization and anchoring of the cytokinetic actin
1211   ring. Mol Biol Cell 16: 3052-63
1212 Venkatram S, Tasto JJ, Feoktistova A, Jennings JL, Link AJ, Gould KL (2004) Identification
1213   and characterization of two novel proteins affecting fission yeast gamma-tubulin complex
1214   function. Mol Biol Cell 15: 2287-301
1215 Weirich CS, Erzberger JP, Berger JM, Weis K (2004) The N-terminal domain of Nup159
1216   forms a beta-propeller that functions in mRNA export by tethering the helicase Dbp5 to
1217   the nuclear pore. Mol Cell 16: 749-60
1218 Wente SR, Rout MP (2010) The nuclear pore complex and nuclear transport. Cold Spring
1219   Harb Perspect Biol 2: a000562
1220 Wu J, Akhmanova A (2017) Microtubule-Organizing Centers. Annu Rev Cell Dev Biol
1221 Wu J, de Heus C, Liu Q, Bouchet BP, Noordstra I, Jiang K, Hua S, Martin M, Yang C,
1222   Grigoriev I, Katrukha EA, Altelaar AF, Hoogenraad CC, Qi RZ, Klumperman J,
1223   Akhmanova A (2016) Molecular Pathway of Microtubule Organization at the Golgi
1224   Apparatus. Dev Cell 39: 44-60
1225 Xu D, Marquis K, Pei J, Fu SC, Cagatay T, Grishin NV, Chook YM (2015) LocNES: a
1226   computational tool for locating classical NESs in CRM1 cargo proteins. Bioinformatics 31:
1227   1357-65
1228 Zebrowski DC, Vergarajauregui S, Wu CC, Piatkowski T, Becker R, Leone M, Hirth S,
1229   Ricciardi F, Falk N, Giessl A, Just S, Braun T, Weidinger G, Engel FB (2015)
1230   Developmental alterations in centrosome integrity contribute to the post-mitotic state of
1231   mammalian cardiomyocytes. Elife 4
1232 Zeitler B, Weis K (2004) The FG-repeat asymmetry of the nuclear pore complex is
1233   dispensable for bulk nucleocytoplasmic transport in vivo. J Cell Biol 167: 583-90
1234 Zhang J, Megraw TL (2007) Proper recruitment of gamma-tubulin and D-TACC/Msps to
1235   embryonic Drosophila centrosomes requires Centrosomin Motif 1. Mol Biol Cell 18: 4037-
1236   49
1237 Zheng L, Schwartz C, Wee L, Oliferenko S (2006) The fission yeast transforming acidic
1238   coiled coil-related protein Mia1p/Alp7p is required for formation and maintenance of
1239   persistent microtubule-organizing centers at the nuclear envelope. Mol Biol Cell 17: 2212-
1240   22
1241
1242

Supplementary Figures

Fig. 1 Supplement 1. Additional data relating to Mto1[NE] and Mto1[bonsai], and Mto1[NE] localization in *alp7Δ*.

Fig. 3 Supplement 1. Additional data relating to leptomycin B sensitivity.

Fig. 4 Supplement 1. Summary of replicate mass spectrometry results comparing GFP-Mto1[9A1-NE]-HTB and GFP-Mto1[ΔNES-9A1-NE]-HTB interactomes.

Fig.5 Supplement 1. Effects of mutant Ran (*spi1* in fission yeast) on cell viability, Mto1[NE] localization, and import of a nuclear localization signal (NLS) reporter

Fig. 6 Supplement 1. Additional characterization of Nup146[ΔFG5-12].

Fig. 7 Supplement 1. Models for stable docking of a high-affinity NES cargo at the cytoplasmic face of the nuclear pore complex via Nup146 and for formation of export-like complexes from cytoplasmic cargo.

Supplementary Files

Supplementary File 1. Yeast strains used in this work.

Supplementary File 2. Mass spectrometry data and summary from preliminary SILAC experiment.

Supplementary File 3. Combined mass spectrometry data and LFQ summaries for experiments shown in Fig. 1.

Supplementary File 4. Combined mass spectrometry data and LFQ summaries for experiments shown in Fig. 3.

Supplementary File 5. Combined mass spectrometry data and LFQ summaries for experiments shown in Fig. 4.

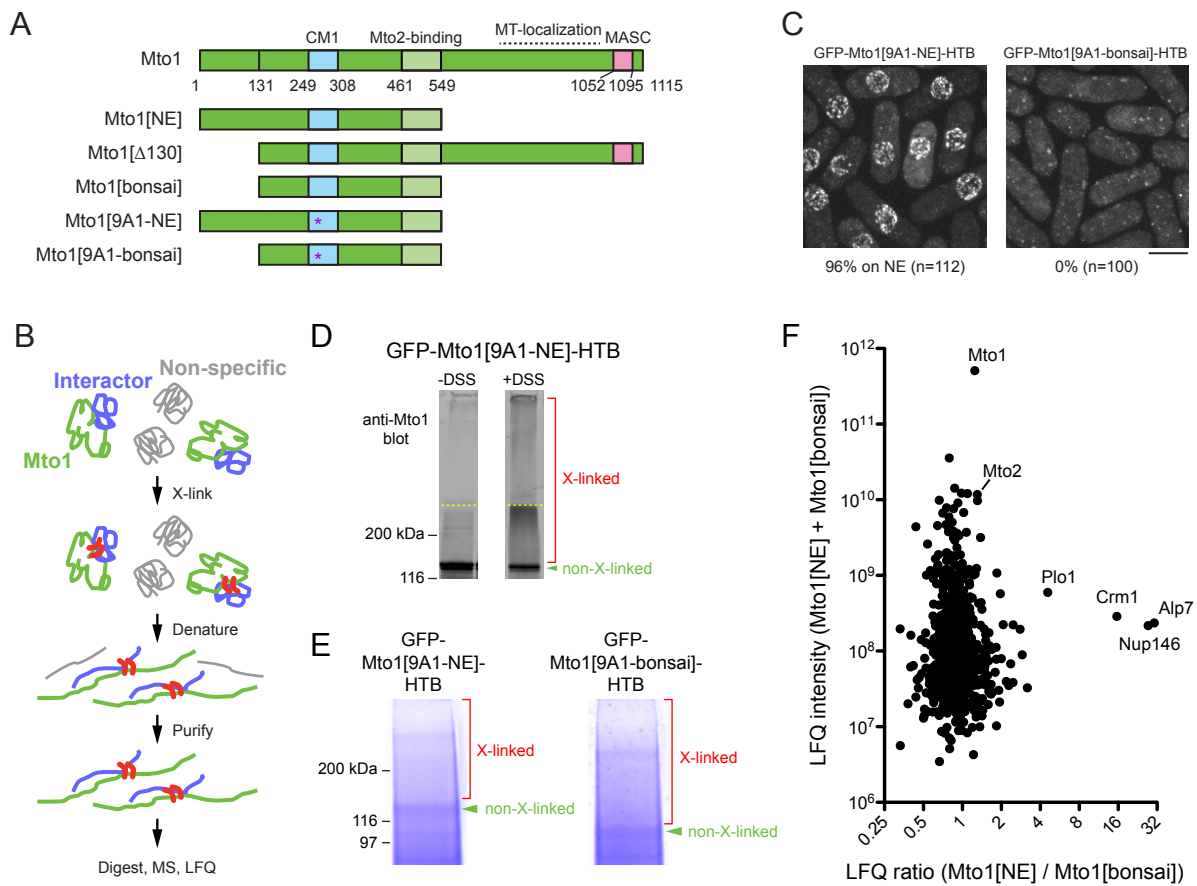**Supplementary File 6.** Combined mass spectrometry data and LFQ summaries for experiments shown in Fig. 6.

Figure 1. Identification of proteins interacting with Mto1[NE] but not Mto[bonsai].
(A) Diagram of full-length Mto1 and Mto1-truncation mutants. Asterisk indicates *9A1* mutation, which abolishes interaction with γ-tubulin complex (Samejima *et al.*, 2008, PMID 19001497). **(B)** Outline of cross-linking and mass spectrometry approach to identify Mto1 interactors. **(C)** Localization of GFP-Mto1[9A1-NE]-HTB and GFP-Mto1[9A1-bonsai]-HTB. Numbers below images indicate percent cells with GFP signal on the nuclear envelope (n= total number of cells scored). **(D)** Anti-Mto1 Western blot of whole-cell lysates from *GFP-mto1[9A1-NE]-HTB* cells in the absence of cross-linking (-DSS) and after disuccinimidyl suberate cross-linking (+DSS). Dashed line indicates boundary between resolving gel and stacking gel. **(E)** SDS-PAGE of GFP-Mto1[9A1-NE]-HTB sample and GFP-Mto1[9A1-bonsai]-HTB sample after DSS cross-linking and two-step denaturing purification. Regions marked "X-linked" were analyzed by mass spectrometry (see Materials and Methods). **(F)** Mass spectrometry label-free quantification (LFQ) of 750 proteins from samples as in E. "LFQ ratio" indicates relative enrichment of a given protein in the purified GFP-Mto1[9A1-NE]-HTB sample compared to the purified GFP-Mto1[9A1-bonsai]-HTB sample. "LFQ intensity" indicates total intensity (arbitrary units) of a given protein from the combined purified samples . Data shown represent one of two independent biological replicates. Complete datasets are in Supplementary File 3. Bar, 5 μm. See also Figure 1 Supplement 1.
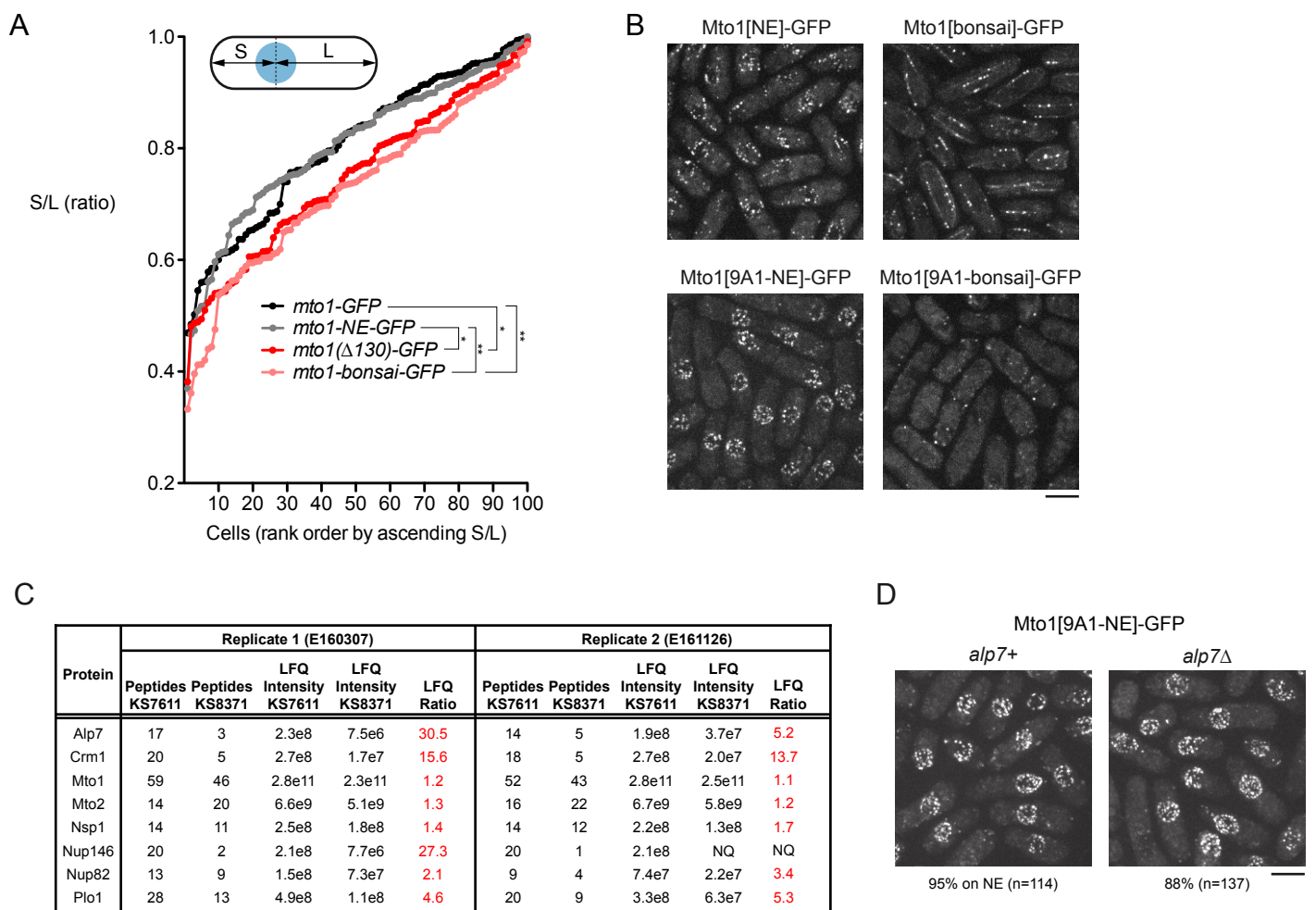
Figure 1 Supplement 1. Additional data relating to Mto1[NE] and Mto1[bonsai], and Mto1[NE] localization in *alp7Δ*. **(A)** Nuclear positioning in strains of the indicated genotypes (see Fig. 1A). 100 cells of each genotype were scored. For each cell, distance from nucleus to each cell end was measured. The shorter of the two distances was termed S, and the longer was termed L. Y-axis shows ratio S/L for cells of each genotype, in rank order. Higher S/L ratios indicate more accurate nuclear centering. * p<0.01; ** p<0.001; other differences were not significant. **(B)** Enhancement of localization of Mto1[NE]-GFP to the nuclear envelope (NE) as a result of the *9A1* mutation (previously described by Lynch *et al*., 2014, PMID 24704079). Both Mto1[NE]-GFP and Mto1[bonsai]-GFP promote microtubule (MT) nucleation by the γ-tubulin complex, and thus both are present at minus ends of individual MTs within MT bundles, even though neither binds directly to the MT lattice. When the *9A1* mutation is introduced, absence of MT nucleation abrogates association with MT minus ends, leading to increased Mto1[9A1-NE]-GFP on the NE. **(C)** Peptide counts and label-free quantification (LFQ) values for selected proteins shown in Fig. 1F. Data from two independent biological replicates are shown, with strain numbers and experiment numbers. Nsp1 and Nup82 are included as likely representative Nup146 interactors, based on homology to budding yeast (Belgareh *et al*., 1998, PMID 9843582). NQ = not quantified, because peptide count in the relevant sample was below threshold for quantification. See also Supplementary File 3. **(D)** Localization of Mto1[9A1-NE]-GFP to the NE in both wild-type (*alp7+*) and *alp7Δ* cells. Numbers below images indicate percent cells with Mto1[9A1-NE]-GFP on the NE (n= total number of cells scored). Bars, 5 μm.
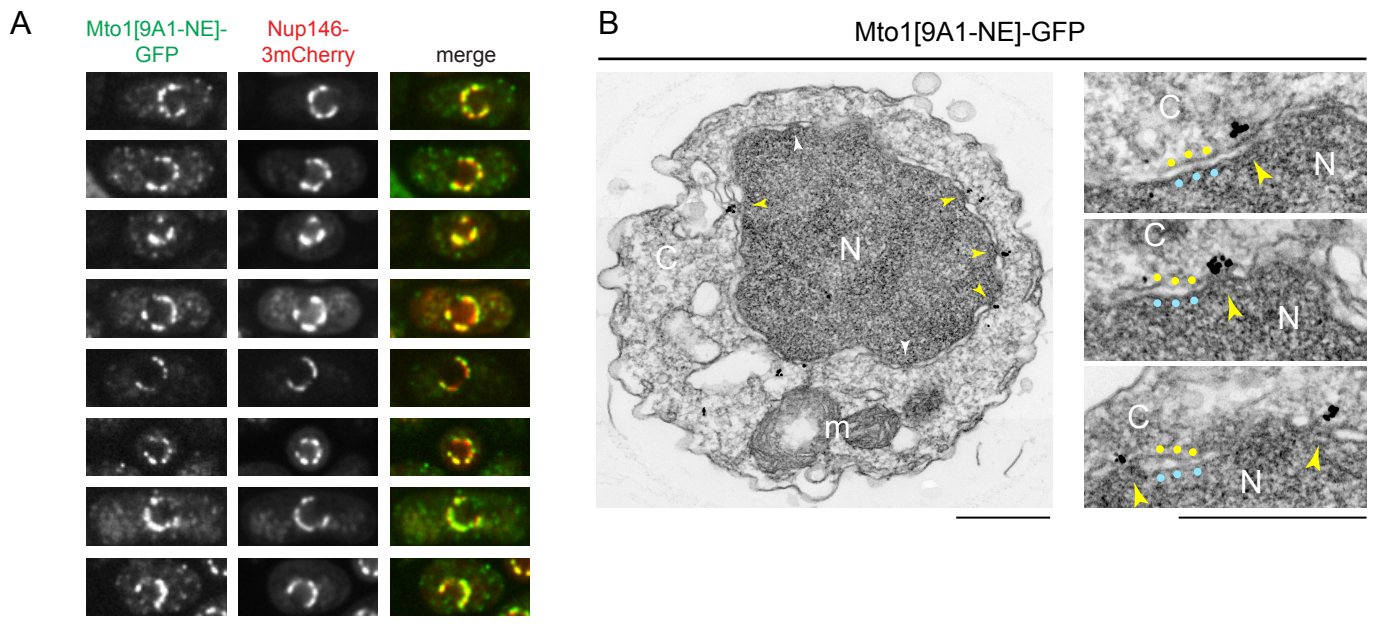
Figure 2. Mto1[NE] is localized to the cytoplasmic face of the nuclear pore complex.
(A) Colocalization of Mto1[9A1-NE]-GFP and Nup146-3mCherry after nuclear pore complex (NPC) clustering in *nup132Δ* cells. For each cell, a single central Z-section is shown. **(B)** Immunoelectron microscopy of Mto1[9A1-NE]-GFP. Left panel shows cross-section of a single cell. NPCs can be seen as slightly electron-dense regions where inner and outer nuclear membranes meet. Yellow arrowheads indicate NPCs with Mto1[9A1-NE]-GFP on cytoplasmic face of NPC. White arrowheads indicate examples of unstained NPCs. Right panels show magnified examples from other cells. Yellow and blue dots indicate inner and outer nuclear membranes, respectively. N, nucleus; C, cytoplasm; m, mitochondria. Bars, 5 μm (A), 0.5 μm (B).
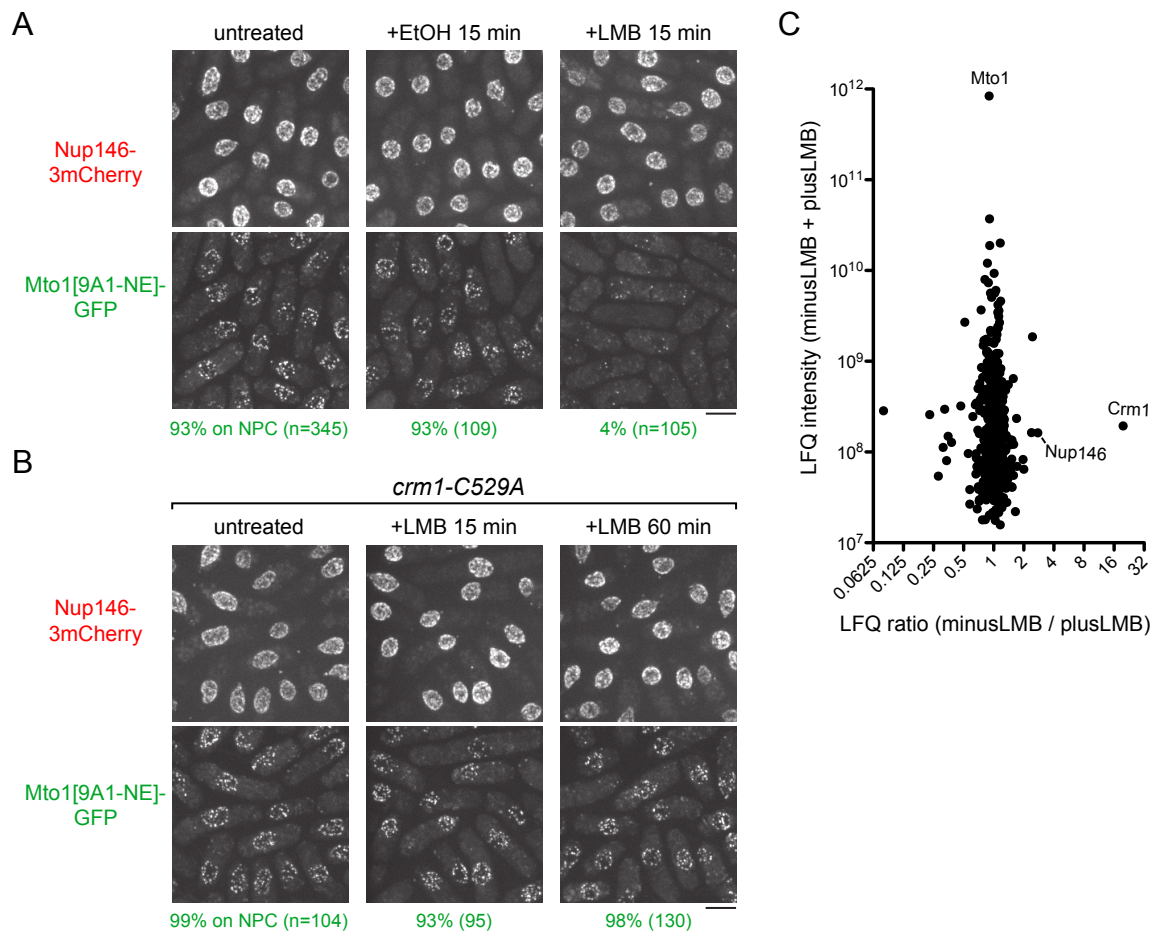
Figure 3. Inhibition of Crm1 cargo-binding by Leptomycin B treatment disrupts Mto1[NE] localization to nuclear pore complexes and Mto1[NE] interaction with Crm1.
(A) Localization of Nup146-3mCherry and Mto1[9A1-NE]-GFP in untreated cells and in cells treated with 1% ethanol (+EtOH) or with 100 nM leptomycin B (+LMB) in ethanol for 15 min. Numbers below images indicate percent cells with Mto1 on NPCs (n=total number of cells scored). **(B)** Localization of Nup146-3mCherry and Mto1[9A1-NE]-GFP in *crm1-C529A* cells, which are resistant to LMB. Cells were untreated or treated with 100 nM LMB for 15 or 60 min. **(C)** Mass spectrometry label-free quantification (LFQ) of 483 proteins from samples of cross-linked, purified GFP-Mto1[9A1-NE]-HTB from untreated ("minusLMB") vs. LMB-treated ("plusLMB") cells. "LFQ ratio" indicates relative enrichment of a given protein in the purified minusLMB sample compared to the purified plusLMB sample. "LFQ intensity" indicates total intensity (arbitrary units) of a given protein from the combined purified samples. Data shown represent geometric mean from two independent biological replicates. See also Figure 3 Supplement 1. Complete datasets are in Supplementary File 4. Bars, 5 µm.

A

-LMB: 18% in N (n=282)
+EtOH 15 min: 28% (88)
+LMB 15 min: 85% (103)
+EtOH 45 min: 22% (94)
+LMB 45 min: 95% (129)

B

C

crm1-C529S: 0% on NPC (n=126)
crm1-C529T: 2% (102)
crm1-C529V: 11% (113)

D

Protein	Replicate 1 (E150924)					Replicate 2 (E151106)				
	Peptides -LMB	Peptides +LMB	LFQ Intensity -LMB	LFQ Intensity +LMB	LFQ Ratio	Peptides -LMB	Peptides +LMB	LFQ Intensity -LMB	LFQ Intensity +LMB	LFQ Ratio
Alp7	20	13	2.5e8	1.4e8	1.7	14	15	6.3e8	4.4e8	1.4
Crm1	17	4	1.1e8	1.3e7	9.0	19	3	2.9e8	6.8e6	43.3
Mto1	59	58	2.6e11	2.9e11	0.9	58	59	6.1e11	6.7e11	0.9
Mto2	7	7	2.0e8	2.2e8	0.9	5	5	6.5e8	8.4e8	0.8
Nsp1	7	7	6.9e7	6.0e7	1.2	11	11	3.7e8	3.7e8	1.0
Nup146	14	8	7.4e7	3.3e7	2.3	12	5	1.9e8	5.6e7	3.4
Nup82	9	10	4.5e7	7.6e7	0.6	9	9	1.7e8	2.9e8	0.6
Plo1	26	26	2.4e8	2.4e8	1.0	25	27	8.5e8	7.7e8	1.1

Figure 3 Supplement 1. Additional data relating to leptomycin B sensitivity.
(A) Localization of Nup146-3mCherry and Alp7-3GFP in untreated cells and in cells treated with 1% ethanol (+EtOH; carrier) or with 100 nM leptomycin B (LMB) in ethanol for 15 and 45 min. Numbers below images indicate percent cells with Alp7 in the nucleus (n=total number of cells scored). Arrowheads indicate examples of Alp7-3GFP accumulation in the nucleus. Brackets indicate examples of Alp7-3GFP puncta on the intranuclear microtubule bundle that forms in interphase cells after LMB treatment (Matsuyama *et al*., 2006, PMID 16823372). **(B)** Colony formation and growth of wild-type cells (*crm1+*) and *crm1* mutants indicated, on plates without LMB and on plates containing 100 nM or 300 nM LMB . While *crm1-C529A*, *crm1-C529T*, and *crm1-C529V* mutants are essentially completely resistant to LMB, *crm1-C529S* mutant is only partially resistant. **(C)** Mto1[9A1-NE]-GFP and Nup146-3mCherry localization in the *crm1* mutants indicated, in the absence of LMB. Unlike *crm1-C529A* (Fig. 3), in these mutants, Mto1[9A1-NE]-GFP fails to localize to nuclear pore complexes. **(D)** Peptide counts and label-free quantification (LFQ) values for selected proteins from the two replicate experiments contributing to the graph in Fig. 3C. Bars, 5 µm. See also Supplementary File 4.

A

LocNES 0.542

1-MEENSSELDSNNFNVLVDNLAGLSLTDEEVRRI-33

LocNES 0.766

B

```
Mto1 12-25    NFNVLVDNLAGLSL
PKI Φ0Leu     NLNELALKLAGLDI
Super-PKI-3   DIDELALKFAGLDL
S1 Φ0Val      DVSDLARLFSALSV
NS2 Φ0Val     TVDEMTKKFGTLTI
```

C

GFP-Mto1[9A1-NE]-HTB

GFP-Mto1[ΔNES-9A1-NE]-HTB

97% on NPC (n=102)   0% (n=128)

D

E

GFP-Mto1[1-29]-GST

GFP-Mto1[1-12]-GST

GFP-Mto1[1-29]-13Myc

93% on NPC (n=99)   0% (n=117)   0% (n=104)

F

GFP-Mto1[1-29]-GST +LMB

0% (n=122)
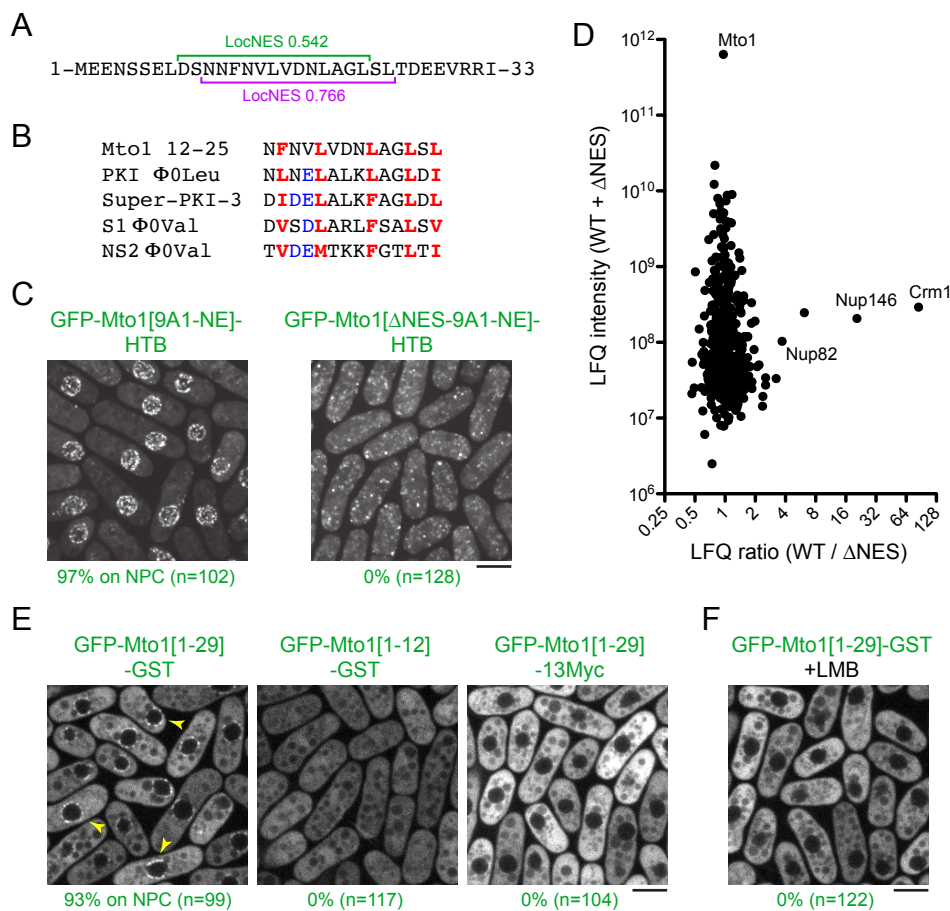
**Figure 4. Mto1 interacts with Crm1 via a NES-like sequence near the Mto1 amino-terminus.**
(A) Predicted NESs in the first 33 amino acids of Mto1, with associated LocNES scores (Xu *et al*., 2015, PMID 25515756). These are the only sequences in the first 130 amino acids of Mto1 with LocNES scores greater than 0.1 **(B)** Alignment of Mto1 amino acids 12-25 with four non-natural, high-affinity NESs ("supraphysiological" NESs) described by Güttler *et al*. (Güttler *et al*., 2010, PMID 20972448; Engelsma *et al*., 2004, PMID 15329671). Conserved hydrophic residues are indicated in red. Acidic residues shown to enhance NES affinity for Crm1 are in blue. **(C)** Localization of GFP-Mto1[9A1-NE]-HTB and GFP-Mto1[ΔNES-9A1-NE]-HTB, which lacks Mto1 amino acids 1-25. Numbers below images indicate percent cells with Mto1 at NPCs (n= total number of cells scored). **(D)** Mass spectrometry label-free quantification (LFQ) of 469 proteins from samples of cross-linked, purified GFP-Mto1[9A1-NE]-HTB ("WT") and cross-linked, purified GFP-Mto1[ΔNES-9A1-NE]-HTB ("ΔNES"). "LFQ ratio" indicates relative enrichment of a given protein in the purified WT sample compared to the purified ΔNES sample. "LFQ intensity" indicates total intensity (arbitrary units) of a given protein from the combined purified samples. Data shown represent one of two independent biological replicates. Nup82 is labeled because it is likely to interact with Nup146, based on homology with budding yeast (Belgareh *et al*., 1998, PMID 9843582). See also Figure 4 Supplement 1. Complete datasets are in Supplementary File 5. **(E)** Localization of the indicated Mto1 fragments fused to GFP at their N-termini and either GST or 13Myc at their C-termini. Arrowheads indicate examples of localization to the NPCs. Numbers below images indicate percent cells with Mto1 at NPCs (n= total number of cells scored). **(F)** Localization of GFP-Mto1[1-29]-GST in leptomycin B-treated cells. Images in E and F are single Z-sections, while other images are maximum projections. Bars, 5 μm.

Protein	Replicate 1 (E160419)					Replicate 2 (E161127)				
	Peptides KS7611	Peptides KS8573	LFQ Intensity KS7611	LFQ Intensity KS8573	LFQ Ratio	Peptides KS7611	Peptides KS8573	LFQ Intensity KS7611	LFQ Intensity KS8573	LFQ Ratio
Alp7	15	14	2.2e8	1.4e8	1.5	12	9	2.1e8	1.4e8	1.5
Crm1	21	2	2.9e8	3.4e6	85.2	20	2	3.5e8	5.5e6	63.4
Mto1	47	47	3.1e11	3.2e11	1.0	40	40	3.1e11	3.2e11	1.0
Mto2	10	10	4.8e9	4.1e9	1.2	8	8	6.3e9	5.9e9	1.1
Nsp1	10	9	2.2e8	1.2e8	1.8	10	9	2.4e8	1.0e8	2.4
Nup146	15	3	2.0e8	9.5e6	20.7	19	0	1.5e8	NQ	NQ
Nup82	10	7	8.1e7	2.2e7	3.7	6	2	5.1e7	NQ	NQ
Plo1	17	15	2.5e8	1.6e8	1.5	17	10	2.2e8	1.8e8	1.2

Figure 4 Supplement 1. Summary of replicate mass spectrometry results comparing GFP-Mto1[9A1-NE]-HTB and GFP-Mto1[ΔNES-9A1-NE]-HTB interactomes.

Peptide counts and label-free quantification (LFQ) values for selected proteins shown in Fig. 4D. Data from two independent biological replicates are shown, with strain numbers and experiment numbers. NQ = not quantified, because peptide count and/or LFQ intensity in the relevant samples was below threshold for quantification. See also Supplementary File 5.
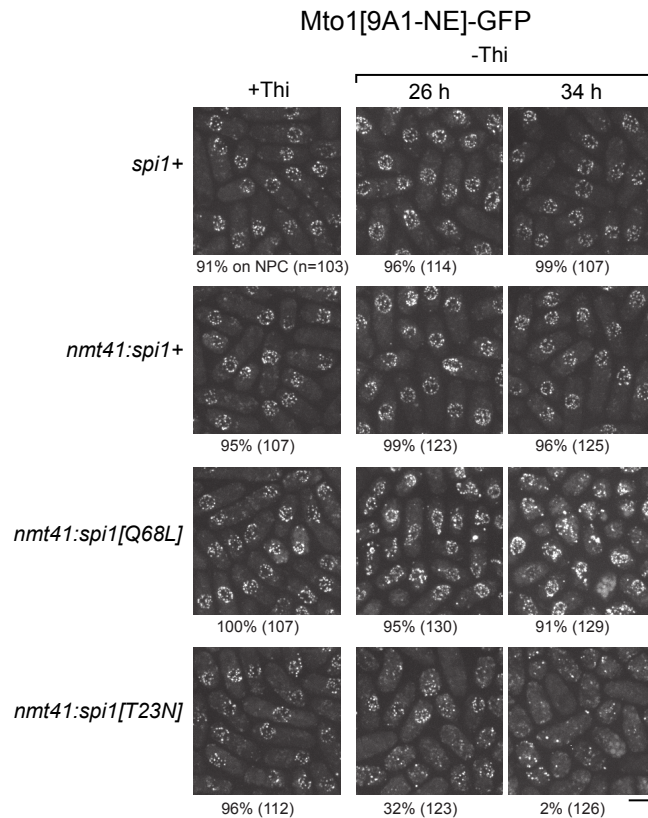
Figure 5. Expression of dominant-negative Ran (*spi1[T23N]*) but not constitutively active Ran (*spi1[Q68L]*) disrupts localization of Mto1[NE] to nuclear pore complexes.
Mto1[9A1-NE]-GFP localization in strains containing different versions of Ran (*spi1* in fission yeast) expressed from the thiamine-repressible *nmt41* promoter, together with control wild-type cells (*spi1+*). Cells are shown in the presence of thiamine (+Thi), and 26 and 34 h after removal of thiamine (-Thi). 26 and 34 h represent early and later stages of induced expression, respectively (see Fig. 5 Supplement 1). Numbers below images indicate percent cells with Mto1[9A1-NE]-GFP on nuclear pore complexes (n=total number of cells scored). Bar, 5 μm.
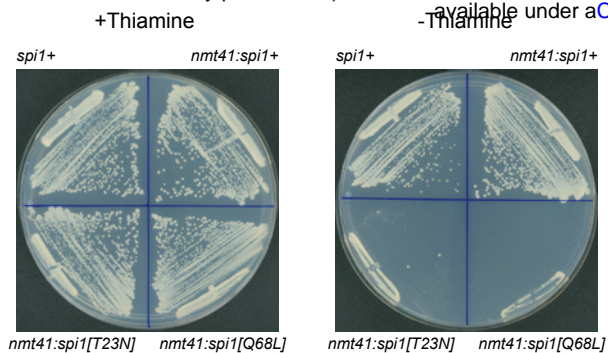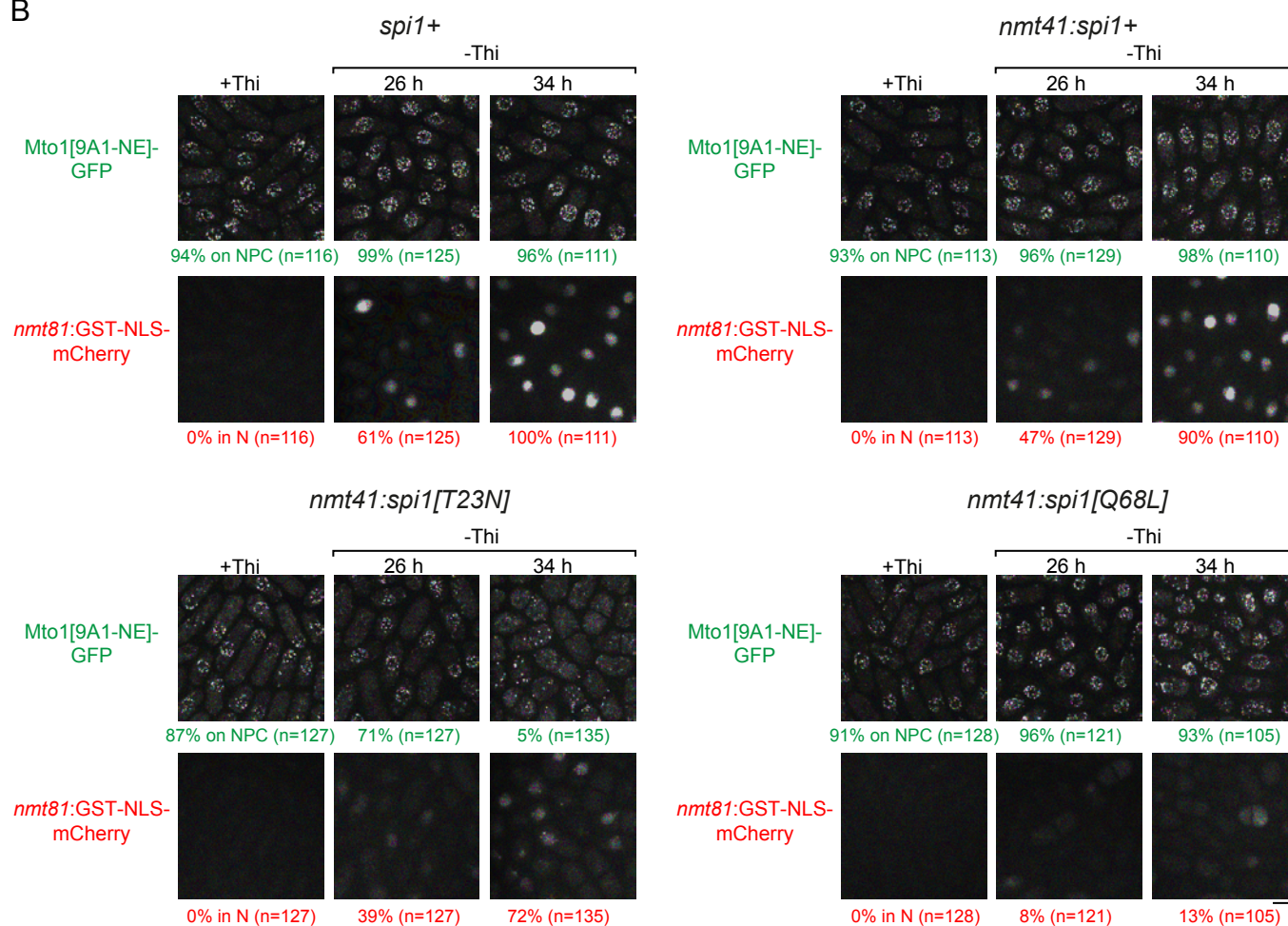
Figure 5 Supplement 1. Effects of mutant Ran (*spi1* in fission yeast) on cell viability, Mto1[NE] localization, and import of a nuclear localization signal (NLS) reporter.
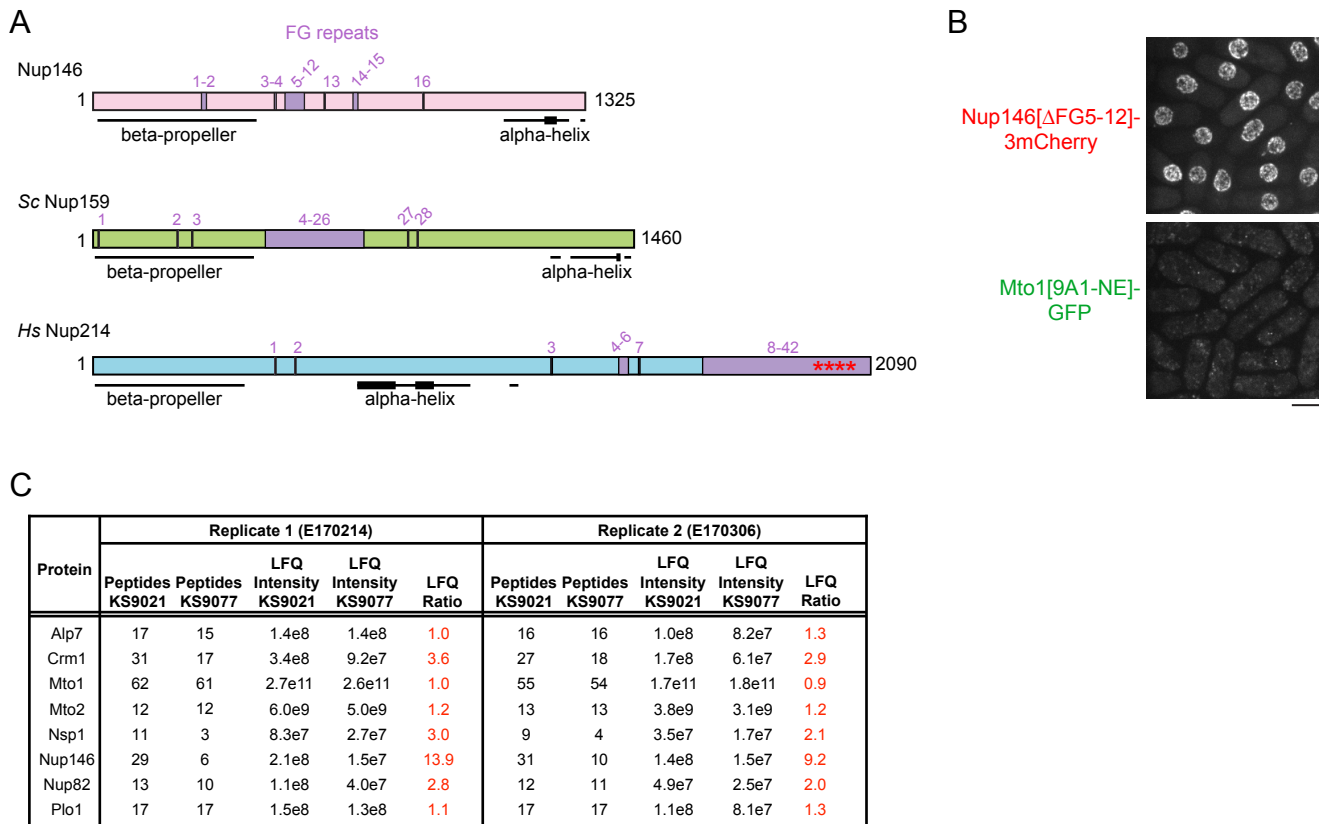
(A) Colony formation after 2 d growth in the presence and absence of thiamine, in (clockwise from top left) control cells (*spi1+*) and cells expressing wild-type Ran (*nmt41:spi1+*), constitutively-active Ran (*nmt41:spi1[Q68L]*), or dominant-negative Ran (*nmt41:spi1[T23N]*), under the control of the medium-strength thiamine-repressible *nmt41* promoter. **(B)** Localization of Mto1[9A1-NE]-GFP, together with nuclear-localization-signal (NLS) reporter GST-NLS-mCherry, in the strains expressing the different versions of Ran. Cells are shown in the presence of thiamine (+Thi), and 26 and 34 h after removal of thiamine to induce expression (-Thi). GST-NLS-mCherry expression is under control of the low-strength thiamine-repressible *nmt81* promoter and thus also regulated by thiamine. Therefore, GST-NLS-mCherry reports both the kinetics of thiamine-regulated expression (e.g. 26 vs. 34 h) and the effects of different Ran mutants on nuclear transport and/or nuclear morphology. Numbers below images indicate percent cells with Mto1[9A1-NE]-GFP on NPCs (green), or percent cells with GST-NLS-mCherry in the nucleus (red; n=total number of cells scored). Images of GST-NLS-mCherry are sum projections, while images of Mto1[9A1-NE]-GFP are maximum projections. Bar, 5 µm.
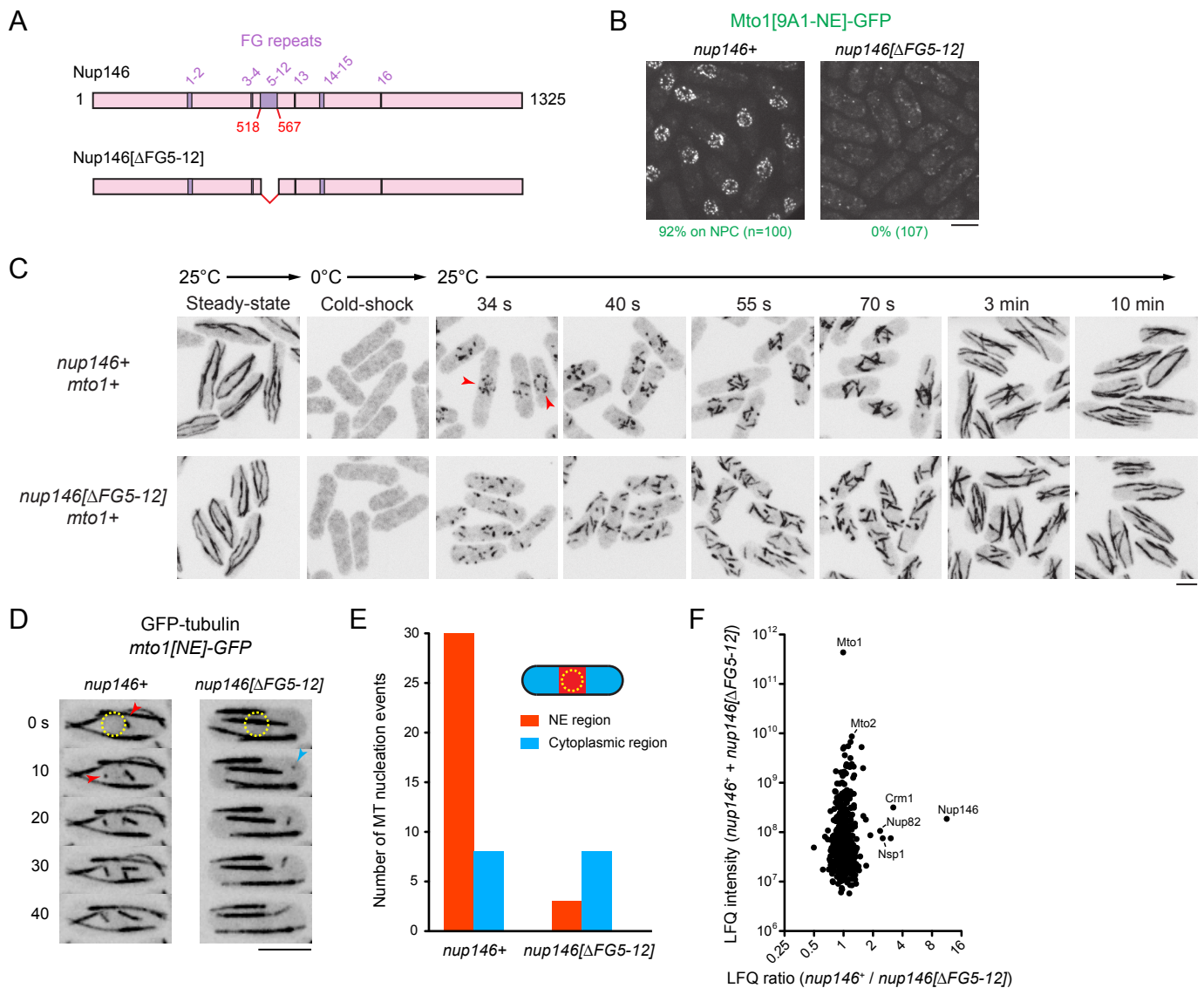
Figure 6. Nup146 FG repeats are required for Mto1[NE] docking at nuclear pore complexes, microtubule nucleation from the nuclear envelope region, and Mto1 interaction with Nup146.
(A) Diagram of Nup146 and Nup146[ΔFG5-12]. **(B)** Localization of Mto1[9A1-NE]-GFP in wild-type (*nup146+*) and *nup146[ΔFG5-12]* cells. Numbers below images indicate percent cells with Mto1 on NPCs (n= total number of cells scored). **(C)** Anti-tubulin immunofluorescence of wild-type (*nup146+)* and *nup146[ΔFG5-12]* cells during microtubule (MT) regrowth after cold-induced MT depolymerization. Both strains express full-length, wild-type Mto1. Arrowheads in *nup146+* cells indicate examples of MT regrowth from the nuclear envelope (NE) region, which does not occur in *nup146[ΔFG5-12]* cells. **(D)** GFP-tubulin images from time-lapse video showing MT nucleation in wild-type (*nup146+*) and *nup146[ΔFG5-12]* cells. Yellow dashed line indicates cell nucleus. Red arrowheads indicate nucleation from the NE region. Blue arrowhead indicates nucleation from non-NE cytoplasmic region. In these cells, Mto1[NE] is also tagged with GFP but is too faint to be seen relative to GFP-tubulin. **(E)** Quantification of MT nucleation from videos of the type shown in D. Numbers represent total number of events for 90 cells of each strain, imaged for 100 s. Differences between strains were highly significant (p=0.0026; Fisher's exact test, two-sided). **(F)** Mass spectrometry label-free quantification (LFQ) of 512 proteins from samples of cross-linked, purified GFP-Mto1[9A1-NE]-HTB from wild-type (*nup146+*) and from *nup146[ΔFG5-12]* cells. "LFQ ratio" indicates relative enrichment of a given protein in the purified sample from *nup146+* cells compared to the purified sample from *nup146[ΔFG5-12]* cells. "LFQ intensity" indicates total intensity (arbitrary units) of a given protein from the combined purified samples. Data shown represent geometric mean from two independent biological replicates. Nup82 and Nsp1 are labeled because they are likely to interact with Nup146, based on homology with budding yeast (Belgareh *et al*., 1998, PMID 9843582). Complete datasets are in Supplementary File 6. Bars, 5 µm. See also Figure 6 Supplement 1.

A — Diagram of Nup146 (1–1325) with FG repeats, beta-propeller and alpha-helix regions; *Sc* Nup159 (1–1460); *Hs* Nup214 (1–2090).

B — Nup146[ΔFG5-12]-3mCherry; Mto1[9A1-NE]-GFP

C

| Protein	Replicate 1 (E170214)					Replicate 2 (E170306)				
	Peptides KS9021	Peptides KS9077	LFQ Intensity KS9021	LFQ Intensity KS9077	LFQ Ratio	Peptides KS9021	Peptides KS9077	LFQ Intensity KS9021	LFQ Intensity KS9077	LFQ Ratio
Alp7	17	15	1.4e8	1.4e8	1.0	16	16	1.0e8	8.2e7	1.3
Crm1	31	17	3.4e8	9.2e7	3.6	27	18	1.7e8	6.1e7	2.9
Mto1	62	61	2.7e11	2.6e11	1.0	55	54	1.7e11	1.8e11	0.9
Mto2	12	12	6.0e9	5.0e9	1.2	13	13	3.8e9	3.1e9	1.2
Nsp1	11	3	8.3e7	2.7e7	3.0	9	4	3.5e7	1.7e7	2.1
Nup146	29	6	2.1e8	1.5e7	13.9	31	10	1.4e8	1.5e7	9.2
Nup82	13	10	1.1e8	4.0e7	2.8	12	11	4.9e7	2.5e7	2.0
Plo1	17	17	1.5e8	1.3e8	1.1	17	17	1.1e8	8.1e7	1.3

Figure 6 Supplement 1. Additional characterization of Nup146[ΔFG5-12].
(A) Diagram of *S. pombe* Nup146 (see Fig. 6), together with homologs *S. cerevisiae* Nup159 and *H. sapiens* Nup214. Note rearranged domain organization in Nup214. All FG (Phe-Gly) sequence repeats are numbered, although some (e.g. near N-terminus) may not interact with nuclear transport receptors. Where FG repeats are too dense to be individually labeled, the corresponding region is labeled. Asterisks in Nup214 indicate structured portion of FG repeats observed in co-crystal with Crm1 (Port *et al*., 2015, PMID 26489467). Beta-propeller structures in *Sc* Nup159 and *Hs* Nup214 have been experimentally verified (Weirich *et al*., 2004, PMID 15574330; Napetschnig *et al*., 2007, PMID 17264208) and are known to bind to RNA helicases *Sc* Dbp5 and *Hs* Ddx19 (respectively), which are involved in mRNP processing in terminal stages of mRNA export. Beta-propeller structure in Nup146 is predicted (Weirich *et al*. 2004). Alpha-helical regions were predicted using JPred4 (Drozdetskiy *et al*., 2015, PMID 25883141). Thicker lines in alpha-helical regions indicate predicted coiled-coils or amphipathic helices. Alpha-helix at the C-terminus of *Sc* Nup159 is involved in forming a heterotrimeric complex with *Sc* Nup82 and *Sc* Nup116 (Yoshida *et al*., 2011, PMID 21930948), whose counterparts in fission yeast are Nup82 and Nup189n, respectively. **(B)** Localization of Nup146[ΔFG5-12]-3mCherry to NPCs, with corresponding localization of Mto1[9A1-NE]-GFP. **(C)** Peptide counts and label-free quantification (LFQ) values for selected proteins from the two replicate experiments contributing to the graph in Fig. 6F. Complete datasets are in Supplementary
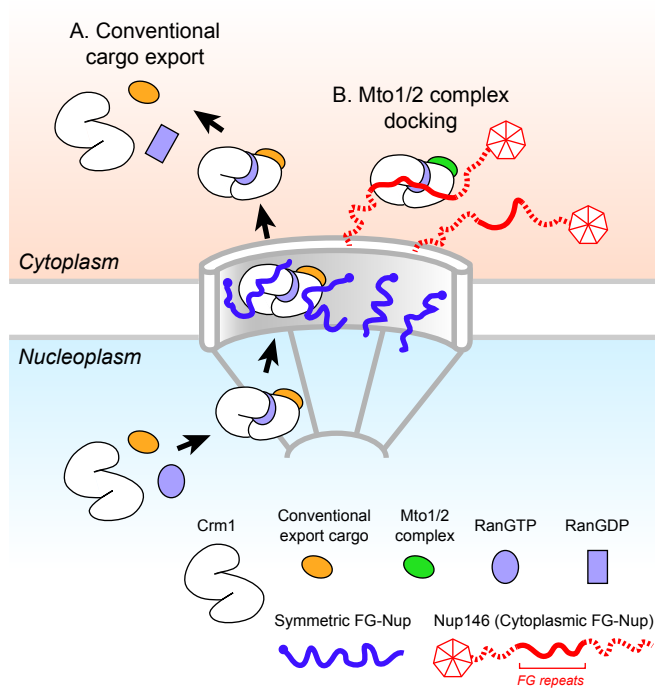
Fig. 7 Model for Mto1/2 complex docking at the nuclear pore complex (NPC), compared to conventional nuclear export

(A) Conventional export cargos form a trimeric complex with Crm1 and RanGTP in the nucleus. Passage through NPC permeability barrier depends on interaction of export complexes with FG repeats of symmetric FG-Nups. While passing through the NPC, some export complexes may also interact with FG repeats of Nup146 (not shown). Once in the cytoplasm, export complexes are disassembled by soluble RanBP1 and RanGAP, and RanGTP is hydrolyzed to RanGDP (here, multiple steps are simplified to a single step). **(B)** Mto1/2 complex docked at NPC. Mto1/2 is sourced from a cytoplasmic pool rather than a nucleoplasmic pool. The Mto1 NES-M binds Crm1 by mimicking an export cargo, and the docking complex binds to cytoplasmic FG-Nup Nup146. Docking requires RanGTP and FG repeats of Nup146. Style of drawing is adapted from Port *et al*. (2015, PMID 26489467). See also Figure 7 Supplement 1.
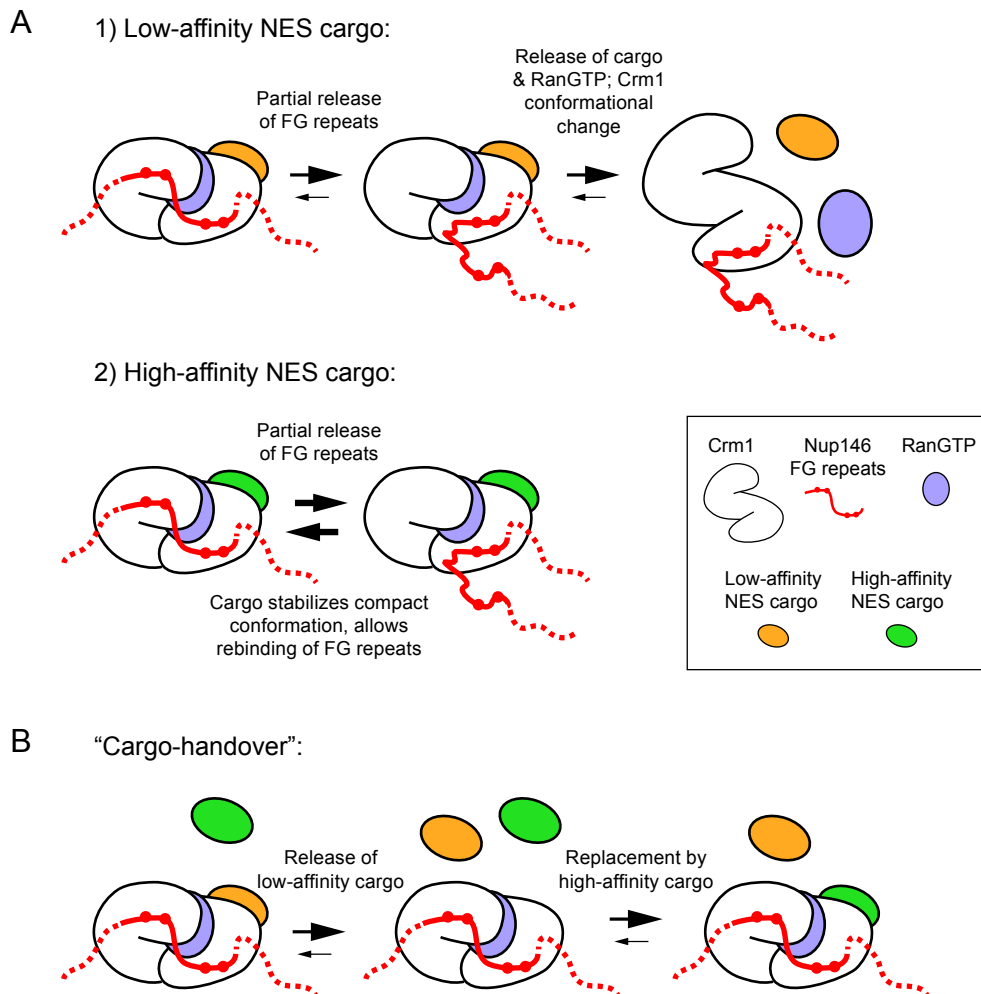
Figure 7 Supplement 1. Models for stable docking of a high-affinity NES cargo at the cytoplasmic face of the nuclear pore complex via Nup146 and for formation of export-like complexes from cytoplasmic cargo.
(A) Speculative model for how a high-affinity NES cargo could become docked at the cytoplasmic face of the nuclear pore complex (NPC). Style of drawing is adapted from Port *et al*. (2015, PMID 26489467). In diagrams, only the FG-repeat region of Nup146 is shown; by analogy to *Sc* Nup159, Nup146 is assumed to be anchored at the cytoplasmic face of the NPC by interaction of its C-terminal domain with partners Nup82 and Nsp1. Binding of Crm1 to cargo, RanGTP and Nup146 FG repeats all contribute cooperatively to Crm1 compact conformation. Therefore, 1) if cargo has only low affinity for Crm1, then after partial release of Nup146 FG repeats from Crm1, the trimeric export complex (Crm1, cargo and RanGTP) can disassemble, releasing cargo into the cytoplasm. However, 2) if cargo has a high affinity for Crm1, then stabilization of the Crm1 compact conformation by cargo binding allows partially released FG repeats to rebind to Crm1. Increased stability of interaction between trimeric complex and Nup146 FG repeats leads to increased residence time at the cytoplasmic face of the NPC. See main text for further details. **(B)** "Cargo-handover" as a potential mechanism for incorporating high-affinity NES cargos from the cytoplasm into export-like complexes at the cytoplasmic face of NPCs. First, a conventional nuclear export complex with a low-affinity NES cargo transiently interacts with Nup146 FG repeats during passage through the NPC. Recent integrated structural analysis in budding yeast suggests that FG repeats of *Sc* Nup159 may be directly adjacent to the symmetric FG-Nups at the centre of the NPC (Fernandez-Martinez *et al*., 2016, PMID 27839866); therefore, even though Nup146 FG repeats are not required for export, some proportion of export complexes could be expected to interact with Nup146 during passage through the NPC. Second, low-affinity cargo dissociates from Crm1, while Crm1 remains bound to Nup146 and to RanGTP. Dissociation of low-affinity cargo could be either spontaneous or aided by RanBP1; in both cases this could occur without dissociation or hydrolysis of RanGTP (Koyama *et al*. 2010, PMID 27839866). In absence of cargo, compact Crm1 conformation (and RanGTP binding) may be partially stabilized by interaction with Nup146 FG repeats, as has been shown for FG repeats of *Hs* Nup214 (Hutten *et al*,. 2006, PMID 16943420). Finally, during a "window of opportunity" before dissociation of Crm1 from Nup146, a high-affinity NES cargo such as the Mto1 NES-M can bind to Crm1 to generate the export-like complex.